Chapter 5

Ocean Models

5.1 Summary

(i) In regard to sea surface temperatures, JMA engages in two high-resolution analyses (MGDSST and HIMSST) based on satellite remote sensing data and *in-situ* observation data to provide real-time ocean information. The former covers the global area with 0.25° horizontal resolution and the latter covers the western North Pacific with higher resolution (0.1°). JMA also conducts analysis based on *in-situ* observation data (COBE-SST) to monitor long-term ocean variations such as El Niño events and global warming.

(ii) JMA launched a global ocean data assimilation system for the monitoring of El Niño and the Southern Oscillation (ENSO) in 1995. The assimilation system was replaced by MOVE/MRI.COM-G in 2008, and was further updated to MOVE/MRI.COM-G2 in 2015, which consists of an ocean general circulation model (MRI.COM) and an objective analysis scheme. Its output, along with atmospheric analysis, is fed to a coupled ocean-atmosphere model for ENSO prediction and seasonal forecasting of climate in Japan.

(iii) Another ocean data assimilation system for the Western North Pacific (MOVE/MRI.COM-WNP) has been operated since 2008 to analyze and predict variations in sea water temperature, salinity and currents associated with eddy-scale oceanic phenomena such as the Kuroshio, the Oyashio and mid-scale eddies in the seas adjacent to Japan. In 2020, as the successor to MOVE/MRI.COM-WNP, JMA launched a new system (MOVE/MRI.COM-JPN) for analysis and prediction of oceanographic sub-meso scale events over the coastal seas around Japan as well as the eddy-scale phenomena.

(iv) JMA operates the Global Wave Model (GWM), the Coastal Wave Model (CWM) and the Wave Ensemble System (WENS) as ocean wave models. All three are based on the MRI-III developed by the Agency's Meteorological Research Institute (MRI). The WENS has been developed to provide probabilistic information on ocean waves in medium-range forecasts. The Shallow-water Wave Model (SWM) is also operated in trial mode to predict ocean waves in bays and near-shore areas around Japan with a higher horizontal resolution of one arc minute.

(v) JMA operates two storm surge models. One covers the Japan region and predicts storm surges generated by tropical and extra-tropical cyclones for the Japanese coast. The other is for the Asian region, and is developed within the framework of the WMO Storm Surge Watch Scheme. Horizontal storm surge maps and time-series charts for selected points are issued to Typhoon Committee Members.

(vi) JMA operates a numerical sea ice model to support sea ice forecasting for the southern part of the Sea of Okhotsk. The model forecasts distributions and concentrations of sea ice with a one-week lead time based on dynamic and thermodynamic equations during the winter season.

(vii) JMA's oil spill prediction model was introduced in 1999. Operation is triggered when a large-scale oil spill occurs offshore. The effects of transport by sea surface winds, ocean waves and sea surface currents, turbulent diffusion, evaporation and emulsification are considered.

5.2 Sea Surface Temperature Analysis

5.2.1 Merged Satellite and *In-situ* Data Global Daily Sea Surface Temperature (MGDSST)

Daily sea surface temperatures (SSTs) in the global ocean on a grid of $0.25 \times 0.25°$ are objectively analyzed to support ocean information services (Kurihara *et al.* (2006)). The data are also used as boundary conditions for atmospheric short- and medium-range prediction models (see Section 3.2 and Section 3.3) and as observational data in the ocean data assimilation system for the Western North Pacific (see Section 5.3). SST data obtained from satellite infrared sensors (NOAA/AVHRR, MetOp/AVHRR) and microwave sensors (Coriolis/WINDSAT,GCOM-W1/AMSR2) are used together with *in-situ* SST observations. Many *in-situ* data are obtained through the Global Telecommunication System, but domestic organizations also provide large amounts of data by e-mail.

Satellite-derived SST anomalies (SSTA) from daily SST climatologies are decomposed into long- and short-time scales with a cutoff period of 53 days and large/middle/small scales with cutoff wavelengths of 580 and 143km. The middle scale is intended to represent SST signals caused by mesoscale (eddy-scale) phenomena, and the small scale is intended to represent sub-mesoscale signals. Signals varying with a period shorter than 27 days are cut off due to the significant data noise they contain. Long-time scale signals represent intra-seasonal variations, and short-time scale signals represent variations influenced by atmospheric conditions such as tropical cyclones.

The large scale and long-time scale components of SSTAs from satellites are calibrated with *in-situ* SSTAs using Poisson's equation (Reynolds (1987)). Space-time optimum interpolation (OI) is applied to each component, and a zero value is adopted as the first guess. Space-time correlation coefficients and RMS values of the first guess error and satellite observation errors are statistically estimated a priori from satellite data using the method of Kuragano and Kamachi (2000). The daily SST is the sum of components of interpolated SSTAs and daily climatologies (Figure 5.2.1).

5.2.2 HIgh-resolution Merged satellite and *In-situ* data Sea Surface Temperature (HIMSST)

SST analysis with high resolution is expected to provide optimal information variables such as boundary conditions for NWP models. Regional daily high-resolution ($0.1 \times 0.1°$) SST analysis for the western North Pacific (HIMSST) began in November 2016. In this work, the HIMSST analysis framework is based on that of MGDSST, in which satellite-derived SSTs are decomposed into several spatio-temporal components and analyzed via optimum interpolation.

In addition to the satellite data used in MGDSST, JMA Himawari-8 L3 SSTs produced with a $0.02 \times 0.02°$ horizontal grid resolution and 10-minute intervals are incorporated into HIMSST analysis. JMA Himawari-8 L3 SSTs are calculated using a quasi-physical algorithm (Kurihara *et al.* (2016)) and masked using JMA's Himawari-8 cloud mask product (Imai and Yoshida (2016)). More frequent geostationary meteorological satellite observation supports shorter time-scale components with cut-off periods from 10 days to 27 days in HIMSST analysis.

NOAA-19 SSTs from AVHRR/LAC (Local Area Coverage) and Himawari SSTs are converted into daily SST anomalies on a $0.1 \times 0.1°$ grid and decomposed into small scale with cut-off wavelengths from 22 to 147 km, which are shorter than those of MGDSST. Figure 5.2.2 shows daily HIMSSTs (left) and MGDSSTs (right) in the seas around Hokkaido, Japan. The HIMSSTs show sharper SST gradients due to the higher grid resolution and application of the shorter wavelength components of NOAA-19 and Himawari-8 SSTs.

HIMSSTs support JMA's ocean information services for the western North Pacific, and have also been used since March 2019 to provide boundary conditions for short-range NWP models such as the Meso-Scale Model (MSM) and the Local Forecast Model (LFM) (Section 3.5, Section 3.7). The analysis data are available from the NEAR-GOOS Regional Real Time Database (https://www.data.jma.go.jp/goos/data/database.html).
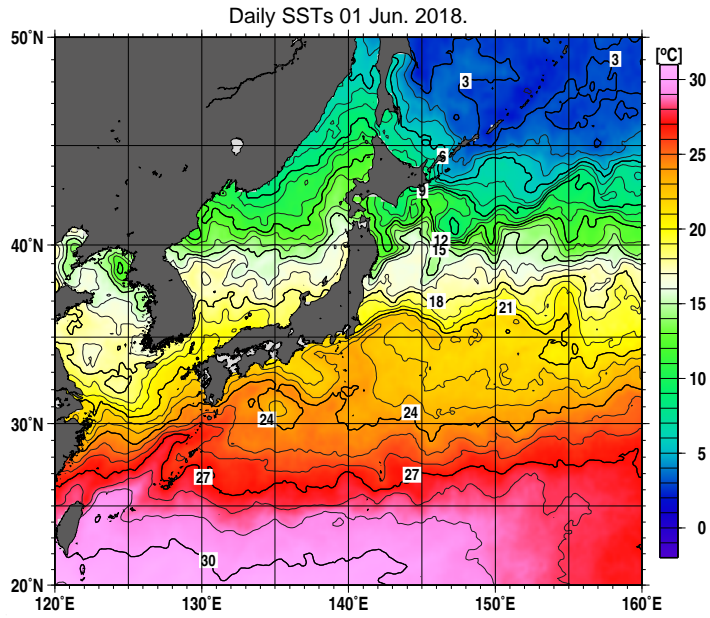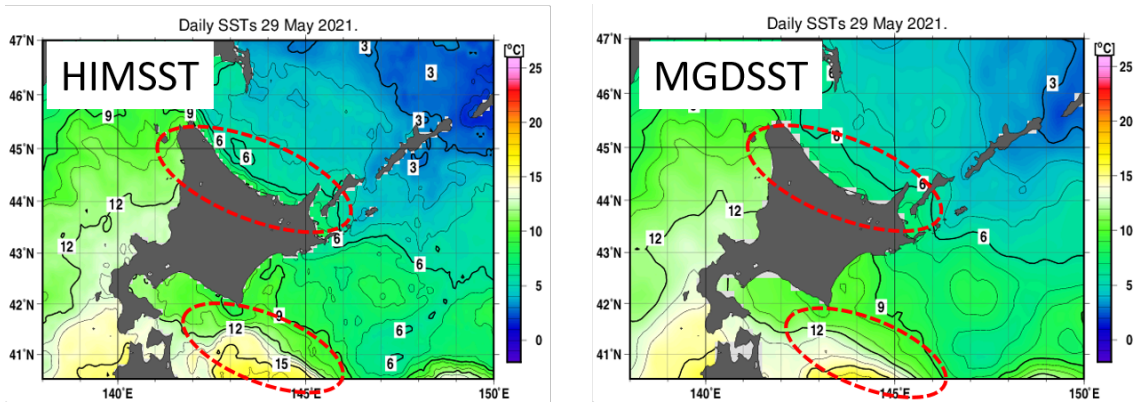
Figure 5.2.1: Sample SST analysis

Figure 5.2.2: Comparison of HIMSST (left) and MGDSST (right) in the seas around Hokkaido.

5.2.3 Daily Sea Surface Analysis for Climate Monitoring

Sea Surface Temperature (SST) analysis for climate monitoring at JMA (COBE-SST) is based on the method described in Ishii *et al.* (2005), which is summarized below.

SST analysis has a resolution of 1° latitude and 1° longitude. The east-west grid points start at 0.5°E and end at 0.5°W. The north-south grid points start at 89.5°S and end at 89.5°N. Analysis is based on the optimum interpolation method, and the deviation of the previous day's analysis from the 1950−2000 normal is multiplied by 0.95 and used as a first guess. Analysis is performed on a daily basis with marine meteorological data for seven days centered on the day of interest. Daily observation data are averaged in $1.5° \times 1.5°$ boxes for analysis using the optimum interpolation method to minimize processing time.

Bias correction for past SST observation reports is based on the method of Folland and Parker (1995). Observation data quality control is performed by checking ship tracks, dates and positions of reports, and erroneous data are automatically corrected in the compilation of marine meteorological data at JMA. Based on observation data deviations from 1950−2000 normals for three months including the day of interest, the biases of data with identical ship call signs are estimated, and call signs associated with large data biases are automatically blacklisted through daily analysis. Daily (final) analysis is performed with a delay of 31 days from real time to allow appropriate use of delayed observations. Daily analysis for the 30-day period following the final analysis is also performed for real-time utilization.

Information on sea ice concentration is used in estimation of SSTs for polar oceans.

The daily updated operational SST data are utilized as described below with historical values.

1. Monitoring of equatorial Pacific SSTs, El Niño/ La Niña evolutions and global warming over 100 years.

2. Input of the operational Ocean Data Assimilation System (MOVE/MRI.COM-G2) and historical oceanic analysis (see Section 5.3).

3. Input of the Japanese 55-year Reanalysis (JRA-55) (see Section 2.10).

Monthly averaged SST data are provided on the Tokyo Climate Center website[1]. The characteristics of the data are described in Japan Meteorological Agency (2006), which is available on the Tokyo Climate Center website[2].

5.3 Ocean Data Assimilation System

JMA has operated multiple systems since 2008 based on a unified ocean data assimilation system MOVE[3]/MRI.COM[4] developed by JMA's Meteorological Research Institute (MRI). These include the global system (MOVE-G) for monitoring of El Niño and the Southern Oscillation (ENSO), which was updated to MOVE-G2 in 2015, and the Western North Pacific system (MOVE-WNP) for analysis of eddy-scale oceanic phenomena in seas around Japan. In 2020, JMA launched MOVE-JPN as the successor to MOVE-WNP for analysis and prediction of oceanographic sub-mesoscale events over coastal areas around Japan and eddy-scale phenomena, and MOVE-WNP will be discontinued in the first half of 2022. The following subsections outline MOVE/MRI.COM and give examples of MOVE-G2, MOVE-WNP and MOVE-JPN operation.

5.3.1 Ocean General Circulation Model and Objective Analysis Scheme

MOVE/MRI.COM consists of an ocean general circulation model (MRI.COM) and an objective analysis scheme (MOVE). MOVE/MRI.COM is described in Usui *et al.* (2006).

MRI.COM (Tsujino *et al.* 2010) is a multilevel model that solves primitive equations under hydrostatic and Boussinesq approximation. The σ-z vertical coordinate system (Hasumi 2006), in which layer thickness near the surface follows surface topography, is adopted in MOVE-G2 and MOVE-WNP to allow free surface

---

[1]https://ds.data.jma.go.jp/tcc/tcc/products/elnino/cobesst/cobe-sst.html
[2]https://ds.data.jma.go.jp/tcc/tcc/products/elnino/cobesst_doc.html
[3]Multivariate Ocean Variational Estimation
[4]Meteorological Research Institute Community Ocean Model

elevation, while the z^* vertical coordinate system (Tsujino *et al.* 2017) is used in MOVE-JPN. For nonlinear momentum advection, a generalized enstrophy-preserving scheme (Arakawa 1972) and a scheme involving the concept of diagonally upward/downward mass momentum fluxes along a sloping bottom are applied. Vertical viscosity and diffusivity are determined using the turbulent closure scheme of Noh and Kim (1999) in MOVE-G2 and MOVE-WNP, and the Generic Length Scale (GLS) scheme (Umlauf and Burchard 2003) representing realistic bottom mixing by tidal currents is used in MOVE-JPN. In MOVE-G2, isopycnal mixing (Gent and McWilliams 1990) is used for horizontal turbulent mixing, and harmonic viscosity with the parameterization of Smagorinsky (1963) is used for momentum. A tracer advection scheme based on conservation of second-order moments (Prather 1986) is adopted in MOVE-G2 and MOVE-JPN. In MOVE-WNP and MOVE-JPN, a biharmonic operator is used for horizontal turbulent mixing, and a biharmonic friction with Smagorinsky-like viscosity (Griffies and Hallberg 2000) is used for momentum. A sea ice model with the thermodynamics of Mellor and Kantha (1989), thickness categories, and ridging and rheology following the Los Alamos sea ice model (CICE; Hunke and Lipscomb 2006) is included in all three systems. Surface forcing to drive the model is based on the Japanese 55-year ReAnalysis (JRA-55, Kobayashi *et al.* (2015); Section 2.11). In MOVE-JPN, atmospheric conditions and sea surface fluxes from the Global Spectral Model (GSM; Yonehara *et al.* (2020); Section 3.2) and the Global Ensemble Prediction System (GEPS, Yamaguchi *et al.* (2020); Section 3.3 are also given, and river runoff from JRA55-do (Tsujino *et al.* 2018) is added to fresh water flux.

The analysis scheme adopted in MOVE-G2 and MOVE-WNP is a multivariate three-dimensional variational (3DVAR) method with vertically coupled Temperature-Salinity (T-S) Empirical Orthogonal Function (EOF) modal decomposition (Fujii and Kamachi 2003). Amplitudes of T-S EOF modes above 1750 m for MOVE-G2 and 1500 m for MOVE-WNP are employed as control variables and the optimal temperature and salinity fields are represented via linear combination of the EOF modes. In these systems, the model domain is divided into several subregions and vertical T-S EOF modes are calculated from the observed T-S profiles for each subregion. The 3DVAR results are inserted into the model temperature and salinity fields via incremental analysis updates (IAU) (Bloom *et al.* 1996) with assimilation windows of 10 days for MOVE-G2 and 5 days for MOVE-WNP. In MOVE-JPN, a four-dimensional variational (4DVAR) analysis scheme is adopted (Usui *et al.* 2015), with the amplitudes of T-S EOF modes above 2000 m as control variables.

These *in-situ* observations are reported from ships, profiling floats and moored or drifting buoys via the GTS and other communication systems. In MOVE/MRI.COM, in-situ observations of temperature and salinity, as well as satellite altimeter data are assimilated into the model. The results of sea surface temperature analysis, performed independently from MOVE/MRI.COM, are also assimilated as observational data. COBE-SST (Ishii *et al.* (2005); Subsection 5.2.2) grid-point values are used for MOVE-G2, and MGDSST (Kurihara *et al.* (2006); Subsection 5.2.1) grid-point values are used for MOVE-WNP and MOVE-JPN.

5.3.2 Ocean Data Assimilation System for Global Oceans (MOVE-G2)

The horizontal resolution is 0.5° latitude and 1.0° longitude except for the 15°S-15°N band, where the latitudinal grid spacing decreases to the minimum of 0.3° between 6°S and 6°N (Figure 5.3.1). The model has 52 vertical levels and a bottom boundary layer (Nakano and Suginohara 2002), 23 of which are placed above 200 m (Figure 5.3.2). The model has realistic bottom topography, and the maximum depth of the bottom is set to 6300 m. The computational domain is the global ocean, including the Arctic Ocean with use of tri-polar horizontal coordinates (Figure 5.3.1). New schemes are introduced in MOVE-G2, such as a bias correction scheme (Fujii *et al.* 2012), a first guess at appropriate time (FGAT) scheme (Lorenc and Rawlins 2005), and a global water mass correction scheme (Kuragano *et al.* 2014).

The latest assimilation results are obtained once every five days, and the targeted term is 3-7 days before assimilation. Assimilation data for the same term are updated every five days using additional delayed-mode observation data until the term reaches 39-43 days before the latest assimilation.

MOVE-G2 output is used in various forms for the monitoring of ENSO at JMA, and products for the equatorial Pacific region are distributed in publications titled Monthly Highlights on the Climate System and El Niño Outlook. Figure 5.3.3 shows one such chart from MOVE-G2 indicating depth-longitude sections of temperature and related anomalies. Report charts are also provided on the Tokyo Climate Center Web page[5].

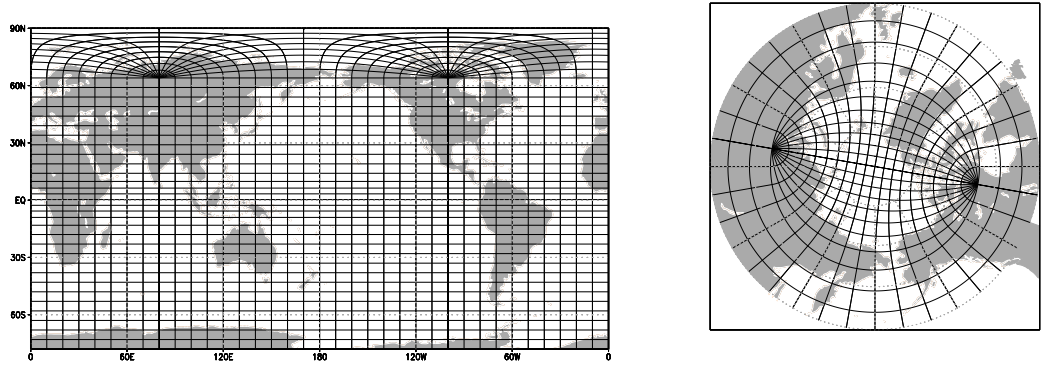[5]http://ds.data.jma.go.jp/tcc/tcc/index.html

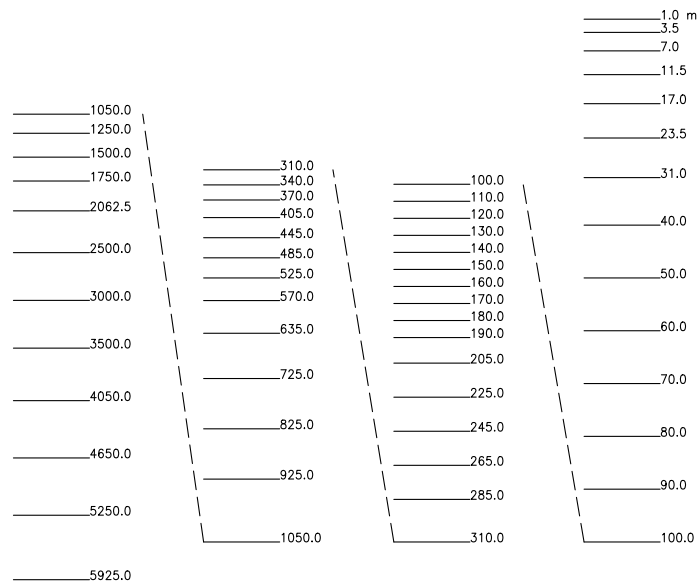Figure 5.3.1: MOVE-G2 horizontal grids. Grid boundaries are shown for every 10 grids

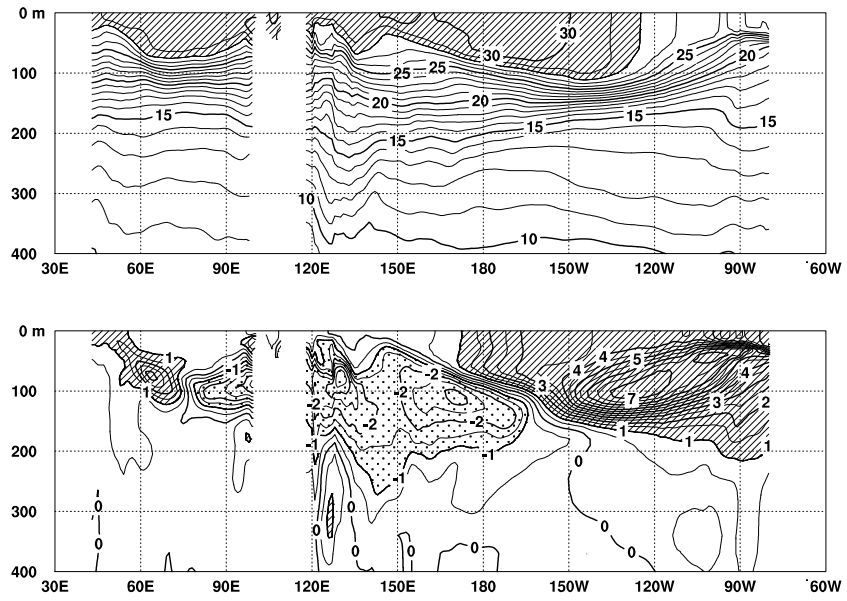Figure 5.3.2: MOVE-G2 vertical levels with depths in meters

Figure 5.3.3: Depth-longitude cross sections of monthly mean temperature and temperature anomalies along the equator in the Indian and Pacific Ocean area for November 2015 based on MOVE-G2. The base period for the normal is 1981–2010.

5.3.3 Ocean Data Assimilation System for the Western North Pacific (MOVE-WNP)

The model domain covers 117°E to 160°W zonally and 15 to 65°N meridionally. The horizontal resolution is variable, with values of 1/10° from 117 to 160°E and 1/6° from 160°E to 160°W, and 1/10° from 15 to 50°N and 1/6° from 50 to 65°N. There are 54 levels in the vertical direction, with thickness increasing from 1 m at the surface to 600 m near the bottom (Figure 5.3.4). Oceanic states at the side boundaries are replaced by those from a North Pacific model with a horizontal resolution of 1/2° (one-way nesting).
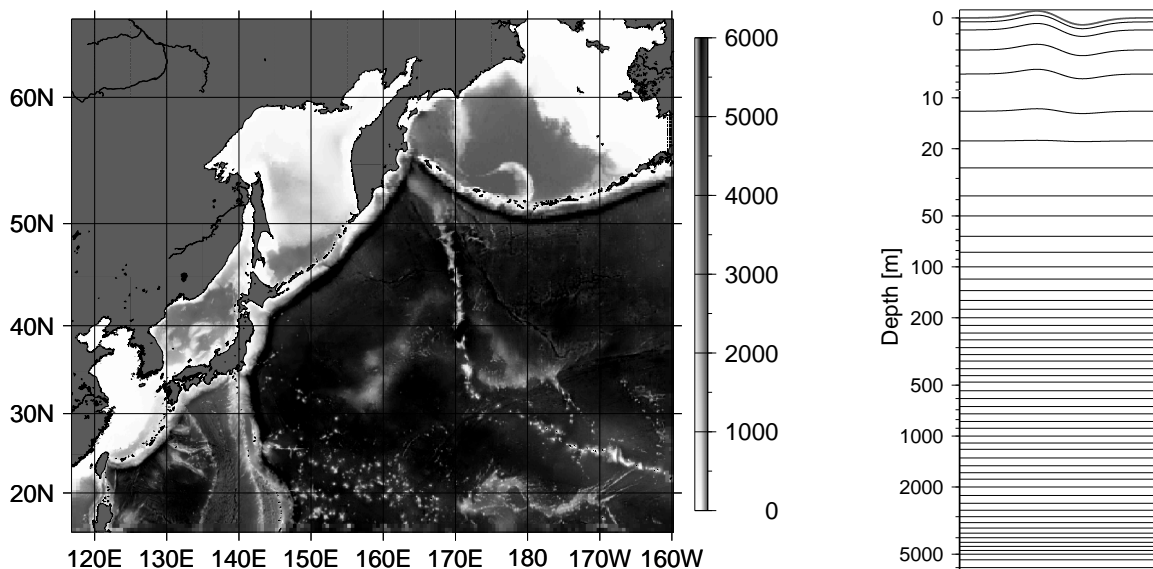

Figure 5.3.4: Bottom topography (left) and vertical levels (right) of the OGCM for the Western North Pacific.

Figure 5.3.5 shows predicted ocean current fields at a depth of 50m as calculated using the forecast run from the initial condition of 9 August 2017. The analysis fields are also shown. It can be seen that the large meander of the Kuroshio path was successfully predicted in the forecast run. The delayed assimilation run is implemented every five days and the prompt assimilation run every day. MOVE-WNP output is used as the initial condition for the ocean forecasting model with a one-month prediction period. The results of operational assimilation and nowcasting/forecasting runs are provided on JMA's web site, and those of assimilation and nowcast runs on the NEAR-GOOS RRTDB[6].

5.3.4 Ocean Data Assimilation and Prediction System for the Seas Around Japan (MOVE-JPN)

MOVE-JPN consists of an analysis system that assimilates ocean observation data and simulates the latest ocean state, and a prediction system that initializes higher-resolution models based on analysis and forecasts the future ocean state.

The analysis system (Hirose *et al.* (2019); Table 5.3.1) consists of a global model (GLB) and a North Pacific model (NPR[7]), both with 60 levels, 31 of which are above 400 m. The GLB has a bottom boundary layer (Nakano and Suginohara 2002) and horizontal coordinates identical to those of MOVE-G2. The NPR model domain spans the area from 99°E to 80°W zonally and 15°S to 63°N meridionally. NPR horizontal resolution is variable, with values of 1/11° from 114°E to 163°E and 1/10° from 17°N to 56°N (≈ 10 km around Japan) and coarser elsewhere. The NPR model (one-way nested within the GLB assimilating global data based on 3DVAR) assimilates observation data based on 4DVAR (Usui *et al.* 2015).

---

[6]https://www.data.jma.go.jp/gmd/goos/data/database.html
[7]The NPR model used for 4DVAR analysis is a reduced-resolution version of the NP model detailed later
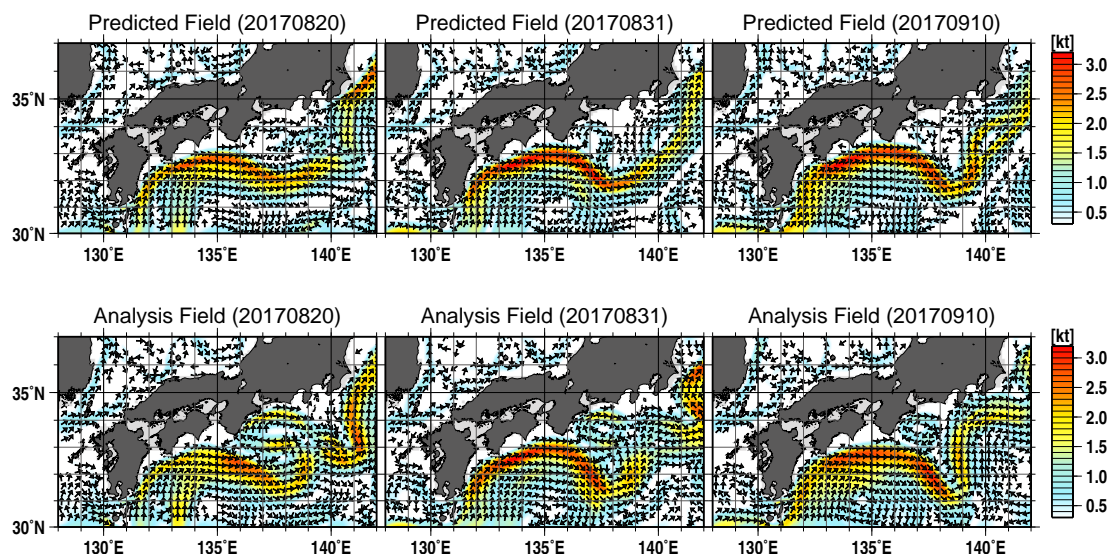
Figure 5.3.5: Horizontal current fields at a depth of around 50m. Top: prediction using the initial condition of 9 August 2017; bottom: assimilation results.

Table 5.3.1: MOVE-JPN analysis system specifications

Basic equations	Primitive with free surface
Numerical technique	Finite difference horizontal and vertical
Model domain	GLB: global NPR: $15°S - 63°N$ between $99°E$ and $75°W$
Nesting	GLB/NPR 1-way off line
Horizontal grid spacing	GLB: $1°$ longitude $\times 0.5°$ latitude NPR: $1/11°$ longitude $\times 1/10°$ latitude for seas around Japan, coarser elsewhere
Vertical levels	60 (GLB with bottom boundary layer)
Number of grids	GLB: $364 \times 366 \times 61 = 8,126,664$ NPR: $1,334 \times 578 \times 60 = 46,263,120$
Tracer advection	QUICK (Leonard 1979)
Vertical turbulent mixing	GLS (Umlauf and Burchard 2003)
Sea ice model	Multicategory ice thickness model with thermodynamic (Mellor and Kantha 1989) and dynamic (Hunke and Lipscomb 2006) components
Sea surface forcing	Heat and water fluxes, surface wind, pressure, temperature, humidity Delayed analysis: from JRA-55 (Kobayashi *et al.* 2015) Prompt analysis: from GSM (Section 3.2)
River runoff	Climatology from JRA55-do (Tsujino *et al.* 2018)
Assimilation	GLB: 3DVAR with 5-day windows NPR: 4DVAR with 10-day windows
Analysis variables	Sea water temperature and salinity above -2,000 m
Sea ice assimilation	Nudging
Observational data	In-situ temperature and salinity above -2,000 m Sea level anomaly (Jason-3, Cryosat-2, Saral; as of 31 March 2021) Sea surface temperature (MGDSST) and sea ice concentration (SSM/I)

Table 5.3.2: MOVE-JPN prediction system specification

Basic equations	Primitive with free surface
Numerical technique	Finite difference horizontal and vertical
Model domain	GLB: global
	NP: 15°S − 63°N, 99°E − 75°W
	JPN: 20° − 52°N, 117° − 160°E
Nesting	GLB and NP: 2-way on line
	JPN: 1-way off line to NP
Grid spacing	GLB: 1° longitude ×0.5° latitude
	NP: 1/11° longitude ×1/10° latitude
	JPN: 1/33° longitude ×1/50° latitude
Vertical levels	60 (GLB with bottom boundary layer)
Number of grids	GLB: $364 \times 366 \times 61 = 8,126,664$
	NP: $2049 \times 784 \times 60 = 96,384,960$
	JPN: $1423 \times 1604 \times 60 = 136,949,520$
Tracer advection	Second-Order Moment (Prather 1986)
Verical turbulent mixing	GLS (Umlauf and Burchard 2003)
Sea ice model	Multicategory ice thickness model with thermodynamic (Mellor and Kantha 1989)
	and dynamic (Hunke and Lipscomb 2006) components
Tidal forcing	8 main tidal constituents
Sea surface forcing	Heat and water fluxes, surface wind, pressure, temperature, humidity
	Eleven-day forecast: from GSM
	Extended forecast: from GEPS (Section 3.3)
River runoff	Climatology from JRA55-do (Tsujino et al. 2018)
Initialization	IAU for 3 days using GLB-3DVAR and NPR-4DVAR results
Sea ice initialization	GLB and NP: nudging to SSM/I
	JPN: nudging to JMA sea ice analysis
Prediction period	GLB and NP: 40 days
	JPN: 11 days

The MOVE-JPN prediction system consists of the GLB, another North Pacific model (NP) and the JPN model (Sakamoto *et al.* (2019); Table 5.3.2). The NP model domain is identical to that of NPR, but its horizontal resolution is zonally 1/11° and meridionally 1/10° over the entire domain (Figure 5.3.6). JPN model domain spans the area 117 − 160°E, 20 − 52°N with grid spacing of around 2 km (zonally 1/33°, meridionally 1/50°). The JPN model is one-way nested to the two-way nested set of the GLB and NP models, all of which explicitly represent tidal motion. NP and JPN are initialized using the IAU scheme with temporal and spatial filtering with temperature and salinity fields from NPR 4DVAR analysis. Using surface boundary conditions output by the GSM, the JPN model forecasts ocean states around Japan with a lead time of 11 days. The two-way nested GLB and NP models continue to forecast ocean states for a month ahead based on GEPS forcing.
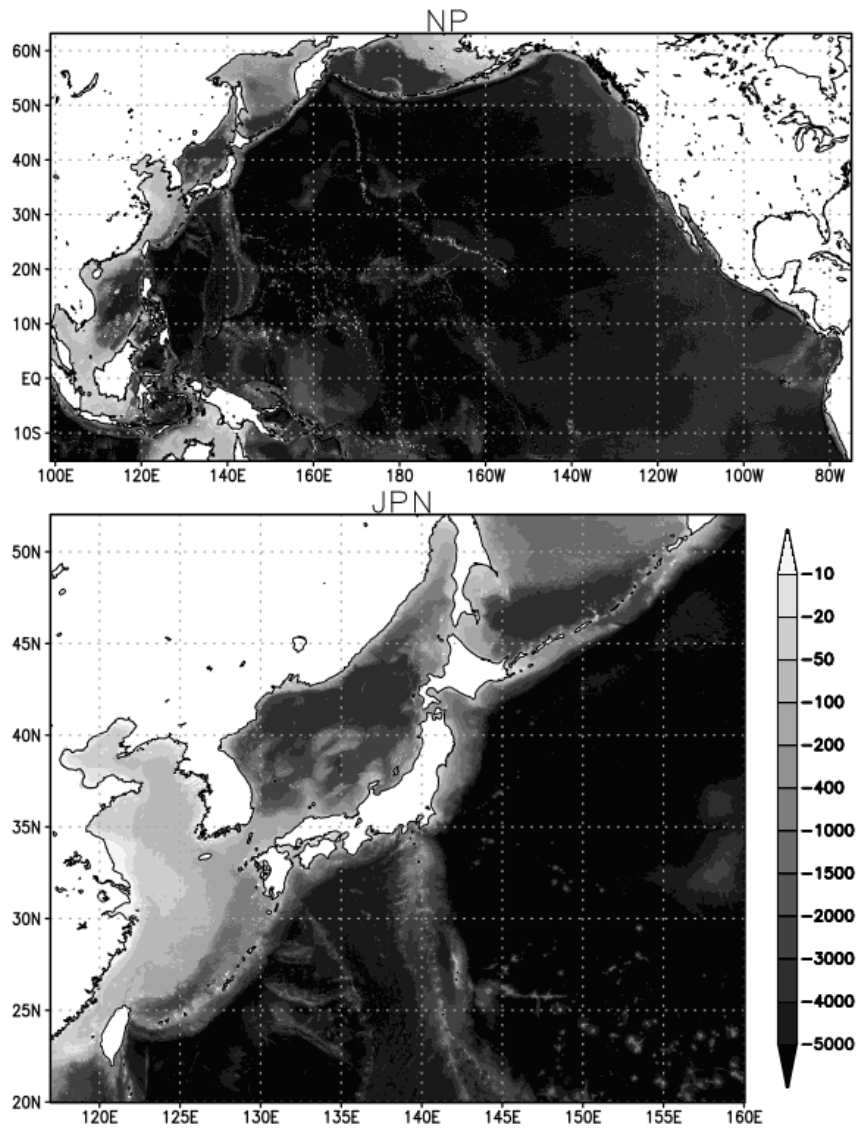
Figure 5.3.6: Bottom topography of the NP model (top) and the JPN model (bottom). The figures show the domain of each model.

Table 5.4.1: Specifications of the Global Wave Model, the Coastal Wave Model and the Wave Ensemble System.

Model name	Global Wave Model	Coastal Wave Model	Wave Ensemble System
Type of wave model	spectral model (third-generation wave model, MRI-III)		
Area	global $75°\text{N} - 75°\text{S}$ $180°\text{W} - 0° - 180°\text{E}$	coastal sea of Japan $50°\text{N} - 20°\text{N}$ $120°\text{E} - 150°\text{E}$	global $75°\text{N} - 75°\text{S}$ $180°\text{W} - 0° - 180°\text{E}$
Grid size	$0.5° \times 0.5°$ (720×301)	$0.05° \times 0.05°$ (601×601)	$0.5° \times 0.5°$ (720×301)
Time step (advection term) (source term)	10 minutes 30 minutes	1 minute 3 minutes	10 minutes 30 minutes
Forecast range (from 06UTC, 18UTC) (from 00UTC) (from 12UTC)	132 hours 132 hours 264 hours	132 hours 132 hours 132 hours	 264 hours 264 hours
Spectral component	900 components 25 frequencies from 0.0375 to 0.3 Hz (logarithmically partitioned) 36 directions		
Initial condition	Analysis by Optimal Interpolation		
Boundary condition		Global Wave Model	
Wind field	Global Spectral Model (GSM)		Global Ensemble Prediction System (GEPS)
	Fujita's empirical formula and a corresponding gradient wind for a typhoon		
Shallow-water effects	Refraction and bottom friction		

5.4 Ocean Wave Models

5.4.1 Introduction

The Japan Meteorological Agency (JMA) operates the Global Wave Model (GWM), the Coastal Wave Model (CWM), and the Wave Ensemble System (WENS). The Shallow-water Wave Model (SWM) is also operated in selected regions.

The GWM, the CWM and the WENS are based on the MRI-III, which was originally developed by the Meteorological Research Institute of JMA (Ueno 2004). The current versions of the GWM and the CWM, which include shallow water effects, have been used for short-range forecasts since May 2017. The WENS, which is a prediction system with probability information and is used for middle-range forecasts, has been in operation since June 2016. The specifications of the three models are given in Table 5.4.1, and their domains are shown in Figure 5.4.1.

The SWM is based on the WAM (The WAMDI Group 1988), but has been modified by the National Institute for Land and Infrastructure Management of the Ministry of Land, Infrastructure, Transport, and Tourism (MLIT) and was put into quasi-operation under a cooperative framework with Water and Disaster Management Bureau of MLIT. It has high resolution of 1 minute (see Table 5.4.2 for specifications), and is applied only to limited areas. The addition of a final 11 areas since 2013, has resulted in today's operation over 22 areas. SWM products are used exclusively within JMA and Regional Development Bureaus of MLIT.

5.4.2 Ocean Wave Model Structure

The ocean wave models forecast the wave energy density (spectrum) of each frequency and direction (i.e., the two-dimensional (directional) wave spectrum). The basic equation is the energy balance expression:

$$\frac{\partial F}{\partial t} + \nabla \cdot (C_g F) + \frac{\partial}{\partial \theta}(\Omega F) = S_{net} = S_{in} + S_{nl} + S_{ds} + S_{btm} \tag{5.4.1}$$
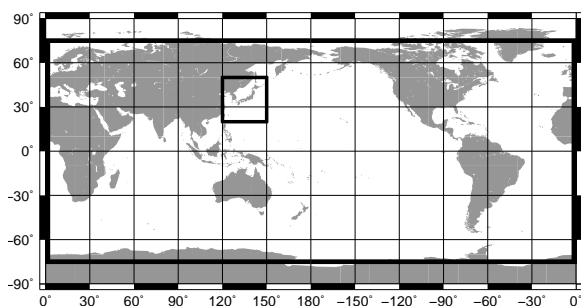
Figure 5.4.1: Calculation areas for the Global Wave Model and the Wave Ensemble System (outer thick lines), and the Coastal Wave Model (inner thick lines).
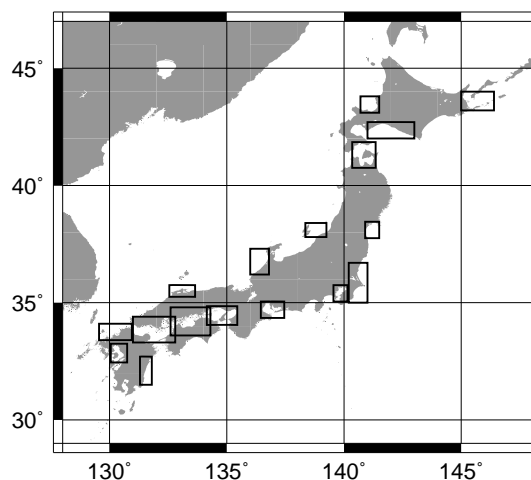

Figure 5.4.2: Calculation areas for the Shallow-water Wave Model.

Table 5.4.2: Specifications of the Shallow-water Wave Model.

Type of wave model	spectral model (third-generation wave model, WAM)					
Areas	Domain name	Grid size	Integration domain	Domain name	Grid size	Integration domain
	Tokyo Bay	37×43	$35.75°N - 35.05°N$ $139.55°E - 140.15°E$	Off Shimane	67×31	$35.75°N - 35.25°N$ $132.55°E - 133.65°E$
	Ise Bay	61×43	$35.05°N - 34.35°N$ $136.45°E - 137.45°E$	Ishikari Bay	49×43	$43.80°N - 43.10°N$ $140.70°E - 141.50°E$
	Harima-Nada Osaka Bay	79×49	$34.85°N - 34.05°N$ $134.15°E - 135.45°E$	Off Ishikawa	49×67	$37.30°N - 36.20°N$ $136.00°E - 136.80°E$
	Ariake Sea Shiranui Sea	43×49	$33.25°N - 32.45°N$ $130.05°E - 130.75°E$	Off Nemuro	85×49	$44.00°N - 43.20°N$ $145.00°E - 146.40°E$
	Off Niigata	55×37	$38.40°N - 37.80°N$ $138.35°E - 139.25°E$	Off Miyazaki	31×73	$32.70°N - 31.50°N$ $131.30°E - 131.80°E$
	Sendai Bay	37×43	$38.45°N - 37.75°N$ $140.90°E - 141.50°E$	Tsugaru Strait	61×67	$41.85°N - 40.75°N$ $140.35°E - 141.35°E$
	Off Tomakomai	121×43	$42.70°N - 42.00°N$ $141.00°E - 143.00°E$	Off Ibaraki Off Boso	49×103	$36.70°N - 35.00°N$ $140.20°E - 141.00°E$
	Suo-Nada Iyo-Nada Aki-Nada	109×67	$34.40°N - 33.30°N$ $131.00°E - 132.80°E$	Genkai-Nada	83×43	$34.10°N - 33.40°N$ $129.55°E - 130.95°E$
	Hiuchi-Nada	103×73	$34.80°N - 33.60°N$ $132.60°E - 134.30°E$			
Grid resolution	$1' \times 1'$					
Time step (advection term) (source term)	1 minute 1 minute					
Forecast range	39 hours					
Spectral component	1260 components 35 frequencies from 0.0418 to 1.1 Hz (logarithmically partitioned) 36 directions					
Initial condition	Coastal Wave Model					
Boundary condition	Coastal Wave Model					
Wind field	Meso-Scale Model (MSM)					
	Fujita's empirical formula and a corresponding gradient wind for a typhoon					

193

where

$$\Omega = \frac{C_g}{C_p}\left(-\frac{\partial C_p}{\partial x}\cos\theta + \frac{\partial C_p}{\partial y}\sin\theta\right),$$

which represents refraction in shallow water. $F(f, \theta, \boldsymbol{x}, t)$ is a two-dimensional spectrum, where f is the frequency and θ is the wave direction, $C_g(f, \theta, \boldsymbol{x})$ is the group velocity, and $C_p(f, \boldsymbol{x})$ is the phase speed. The group velocity is simply $C_g(f)$ for deep-water waves but depends on water depth for shallow-water waves. S_{net} is a net source function consisting of S_{in}, S_{nl}, S_{ds}, and S_{btm}, which are briefly outlined below. Only the model numerics of the MRI-III are described here, as those of the WAM are already extensively referenced elsewhere (e.g. Janssen 2004).

1. S_{in}: energy input from wind. This value generally takes the form $S_{in} = A + BF$, where A is linear wave growth and BF is exponential growth. In the MRI-III, the formula of Cavaleri and Rizzoli (1981) is used for linear growth

$$A = 1.5 \times 10^{-3}\left(u_*^4/2\pi g^2\right)\exp[-(f_{PM}/f)^4]\,(\max(0, \cos(\theta - \theta_W)))^4 \qquad (5.4.2)$$

where u_* is the friction velocity of wind, θ_W is the wind direction, and g is the gravitational acceleration. In general, the linear term has little influence on wave growth except in the very early stages. Meanwhile, the exponential term BF has a key role in wave growth. In the MRI-III, The B is expressed as

$$B(f, u_*, \theta_W - \theta) = c_{in}\left(\frac{u_*}{C_{pd}}\right)^2 f\cos^3(\theta_W - \theta)/|\cos(\theta_W - \theta)|. \qquad (5.4.3)$$

where C_{pd} is the phase speed of deep water waves, i.e., $C_{pd} = \dfrac{g}{\omega} = \dfrac{g}{2\pi f}$.

This expression is based on Mitsuyasu and Honda (1982) and Plant (1982).

2. S_{nl}: nonlinear energy transfer associated with resonant interaction. Since rigorous calculation is highly time-consuming, a practical scheme known as discrete interaction approximation (DIA) (Hasselmann *et al.* 1985) is commonly used in operational wave models. This approach involves the use of only one parameter for the set of four resonant waves:

$$\left.\begin{aligned}
&f_1 = f_2 = f, \\
&f_3 = f(1 + \lambda) = f_+, \\
&f_4 = f(1 - \lambda) = f_-, \\
&\theta_1 = \theta_2 = \theta, \\
&\theta_3 - \theta = \pm\cos^{-1}\left\{\left(1 + 2\lambda + 2\lambda^3\right)/(1 + \lambda)^2\right\}, \\
&\theta_4 - \theta = \mp\cos^{-1}\left\{\left(1 - 2\lambda - 2\lambda^3\right)/(1 - \lambda)^2\right\}.
\end{aligned}\right\} \qquad (5.4.4)$$

$$\left\{\begin{array}{c}\delta S_{nl} \\ \delta S_{nl}^+ \\ \delta S_{nl}^-\end{array}\right\} = \left\{\begin{array}{c}-2(\Delta f\Delta\theta)/(\Delta f\Delta\theta) \\ (1 + \lambda)(\Delta f\Delta\theta)/(\Delta f_+\Delta\theta) \\ (1 - \lambda)(\Delta f\Delta\theta)/(\Delta f_-\Delta\theta)\end{array}\right\}$$

$$\times Cf^{11}g^{-4}\left[F^2\left\{\frac{F_+}{(1 + \lambda)^4} + \frac{F_-}{(1 - \lambda)^4}\right\} - 2\frac{FF_+F_-}{(1 - \lambda^2)^4}\right] \qquad (5.4.5)$$

where $F \equiv F(f, \theta)$, $F_+ \equiv F(f_+, \theta_3)$, $F_- \equiv F(f_-, \theta_4)$. The coefficient C is determined to fit exact calculation for the JONSWAP spectrum. Hasselmann *et al.* (1985) defined the related parameters as $\lambda = 0.25$, corresponding to $\theta_3 - \theta = \pm 11.5°$, $\theta_4 - \theta = \mp 33.6°$ and $C = 3 \times 10^7$. DIA calculation is found to support highly accurate estimation if multi parameters are conbined. In the MRI-III, S_{nl} is calculated using the DIA scheme with three configurations. The parameters used are $\lambda_1 = 0.19\,(C_1 = 1.191 \times 10^7)$, $\lambda_2 = 0.23\,(C_2 = 6.835 \times 10^6)$, and $\lambda_3 = 0.33\,(C_3 = 1.632 \times 10^6)$.

3. S_{ds}: energy dissipation associated with wave breaking and other effects. In the MRI-III, dissipation terms are expressed as local energy dissipation as proposed by Ueno (1998).

$$S_{ds} = -c_b \frac{u_*}{g^3} f^7 \left(F(f, \theta)\right)^2 \tag{5.4.6}$$

where c_b is a coefficient determined to fit wave generation. In the MRI-III, a slightly artificial swell decay process is included.

$$S_{sds} = -2.96 \times 10^{-6} \tanh\left[4\left(f_s - f\right)/f_p\right] F(f, \theta), \tag{5.4.7}$$

where $f_p = 0.156 g/U_{10N}$ represents the peak frequency of the Pierson-Moskowitz (PM) spectrum from the 10m height wind speed U_{10N}. This decay function is applied to the spectrum of frequencies lower than $f_s = 1.8 f_p$ when the significant wave height exceeds 1.5m.

4. S_{btm}: the energy loss associated with bottom friction. This effect needs to be considered for shallow water. In the MRI-III, this term is taken from Hasselmann *et al.* (1973).

$$S_{btm} = -\frac{0.038}{g^2} \cdot \frac{(2\pi f)^2}{\sinh^2(kd)} \cdot F(f, \theta) \tag{5.4.8}$$

where k is the wave number and d is depth. Energy loss increases for shallow water and long-period waves.

5.4.3 Wind Field

Wind fields for the GWM and the CWM are given by the Global Spectral Model (GSM), while the SWM uses Meso-Scale Model (MSM) winds. For the WENS, 51-member wind fields of the Global Ensemble Prediction System (GEPS) are employed.

In the GWM, the CWM and the SWM, wind fields around typhoons are modified using an empirical method. As typhoons contribute significantly to extremely high waves in the western North Pacific, accurate wave forecasts are crucial to the prevention of shipwrecks and coastal disasters. Since NWP models occasionally fail to predict typhoon conditions such as intensity and location accurately, wind fields based on operational typhoon analysis and forecasting are imposed onto NWP winds (known as bogus wind) when a typhoon is present over the western North Pacific. Changes in the course of a typhoon may also result in drastic wave field alterations, especially in the small region covered by the SWM. Accordingly, wave fields are also predicted with the typhoon assumed to move along a five-point path (center, faster, slower, right end and left end) in the typhoon forecast error circle.

To create bogus wind data, sea level pressure distribution near a typhoon is assumed to have a profile expressed by Fujita's empirical formula (Fujita 1952)

$$P(r) = P_\infty - \frac{P_\infty - P_0}{\sqrt{1 + (r/r_0)^2}} \tag{5.4.9}$$

where P_∞, P_0 and r_0 denote the ambient pressure, the central pressure of the typhoon, and the scaling factor of the radial distribution of the pressure, respectively. Surface winds near the typhoon are estimated from the pressure field by assuming the gradient wind balance with modifications based on the typhoon movement and surface friction effects.

5.4.4 Wave Analysis

An assimilation scheme (Kohno *et al.* 2012) for the GWM and the CWM was introduced in October 2012. In these models, initial conditions (wave spectra) are modified based on significant wave heights under the Objective Wave Analysis System (OWAS) (Kohno *et al.* 2009), which objectively analyzes wave heights using optimal interpolation (OI) with observations from radar altimeters of satellites, buoys, coastal wave recorders

Table 5.4.3: JMA Objective Wave Analyses System specifications.

Analysis scheme	Optimal interpolation
Data cut-off time	6 hours and 25 minutes for early run analysis
	12hours for delayed analysis
First guess	6-hour forecast by the GWM and the CWM
Analysis variables	Significant wave height
Grid size	0.5°×0.5° grid for the GWM,
	0.05°×0.05° grid for the CWM
Integration domain	Global oceans for the GWM,
	Coastal sea of Japan for the CWM
Observational data	0.25°×0.25° grid super-observational data from BUOY, SHIP, Nowphas, GPS wave meter, Jason-3,
	SARAL, and Sentinel-3A/B
Assimilation window	6 hours

and ships. The specifications are shown in Table 5.4.3. Introduction of data assimilation improves the prediction of ocean wave fields, especially in terms of shorter forecast times and swell propagation.

5.4.5 Products

JMA issues many ocean wave products based on GWM, CWM, and WENS data.

Ocean wave forecast products based on GWM are provided on activities of RSMCs for numerical ocean wave prediction. These products are available on JMA's website[8].

Charts of analysis and 24-hour ocean wave forecasts are served twice a day via the JMH radio facsimile broadcast service and the JMA website for the Western North Pacific and seas around Japan (Figure 5.4.3). The charts indicate significant wave heights, peak wave directions, and peak wave periods. In addition, information on rough sea areas, that may hinder maritime navigation was incorporated for forecast charts in 2017. The areas of horizontal hatching in Figure 5.4.3(a) indicate areas of crossing waves that may give rise to unexpectedly high-sea conditions. The areas of vertical hatching in Figure 5.4.3(b) show areas in which wave heights and steepness increase due to the effects of opposing ocean currents.

Statistical products detailing significant wave heights and peak wave periods with probability for medium-range forecasts are produced from WENS output and provided on the JMA website for the WMO Severe Weather Forecasting Programme (SWFP[9]) and on the Numerical Typhoon Prediction (NTP) website for Typhoon Committee members. Figure 5.4.4-Figure 5.4.7 show examples for TY Surigae (2102).

---

[8]https://www.jma.go.jp/jma/en/NMHS/JMA_RSMC.html
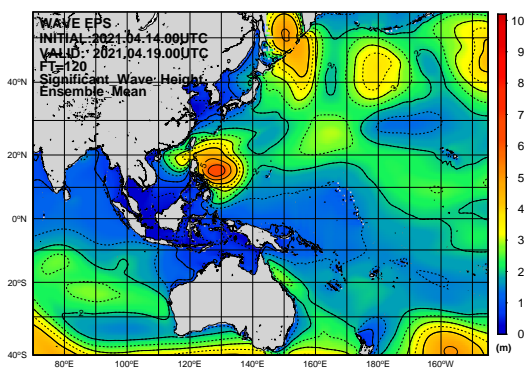[9]https://www.wis-jma.go.jp/swfdp/
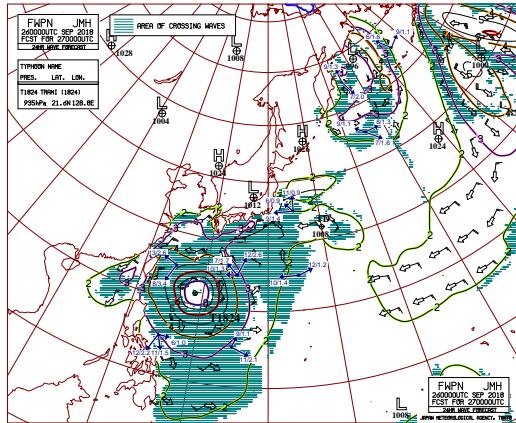
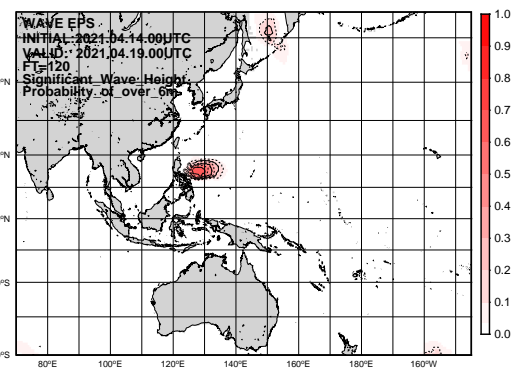(a) Wave forecast chart for the Western North Pacific (FWPN) created from the GWM.
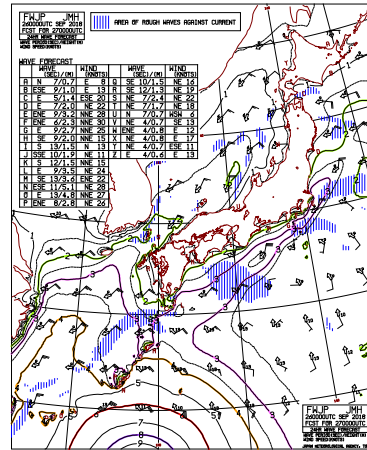
(b) Wave forecast chart for coastal region of the Japan (FWJP) created from the CWM.

Figure 5.4.3: Wave forecast charts based on 24-hour model predictions at the initial time of 00UTC 26 September 2018.
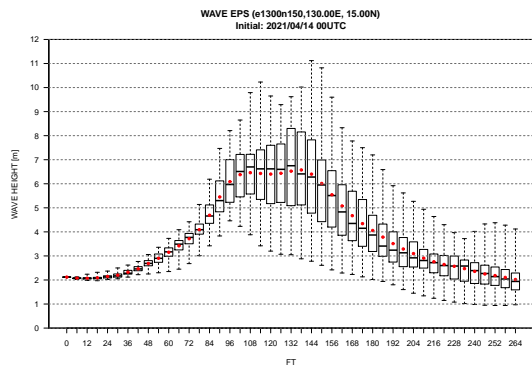

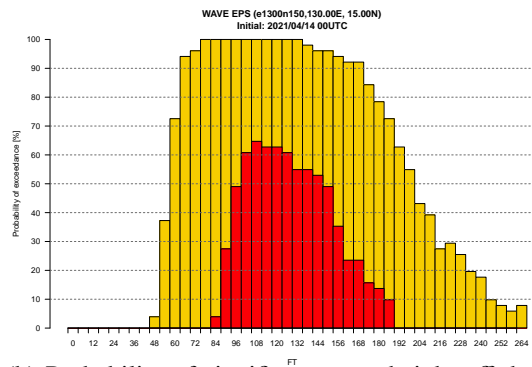(a) Ensemble mean of significant wave height.

(b) Probability of significant wave height over 6m.

Figure 5.4.4: Statistics on significant wave height from 120-hour WENS predictions at the initial time of 00UTC 14 on April 2021.

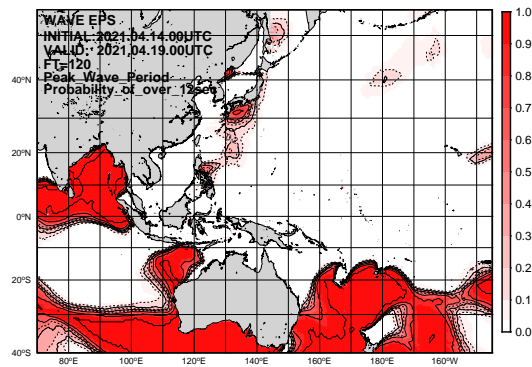(a) Boxplots of significant wave height off the east coast of the Philippines.

(b) Probability of significant wave height off the east coast of the Philippines. Yellow > 3m, Red > 6m.

Figure 5.4.5: Time-series representation of significant wave height from WENS prediction at the initial time of 00UTC 14 on April 2021.
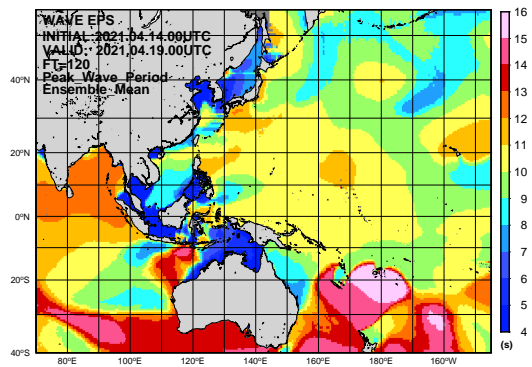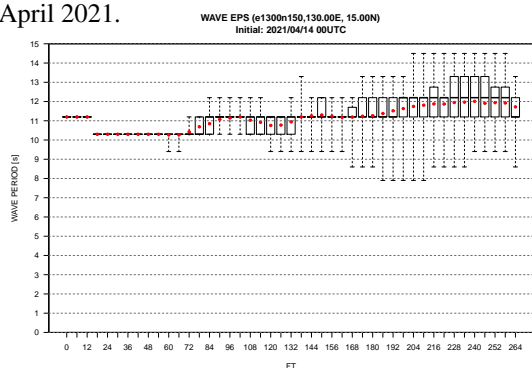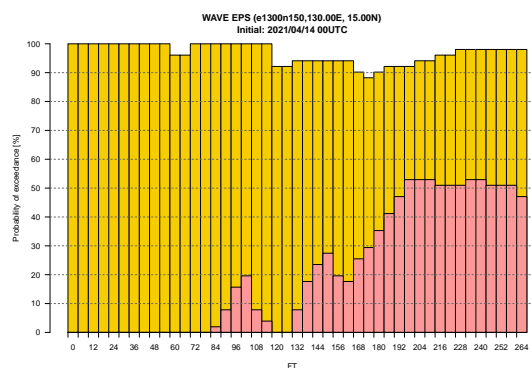

(a) Ensemble mean of wave period.

(b) Probability of wave period over 12sec.

Figure 5.4.6: Statistics on peak wave period from 120-hour WENS predictions at the initial time of 00UTC 14 on April 2021.

(a) Boxplots of wave period off the east coast of the Philippines.

(b) Probability of wave period off the east coast of the Philippines. Yellow > 10sec, Pink > 13sec, Red > 15sec.

Figure 5.4.7: Time-series representation of peak wave period from WENS predictions at the initial time of 00UTC 14 on April 2021.

198

5.4.6 Improvement and Development

The main improvements made to JMA ocean wave models since 2017 are as follows:

1. The shallow water effect was introduced into the GWM and the CWM in 2017, and the WENS in 2020.

2. The horizontal resolution of the WENS was enhanced from 1.25° to 0.5° in 2020.

3. The number of WENS members was increased from 27 to 51 in 2021.

Figure 5.4.8 shows monthly root mean square errors (RMSEs) for the significant wave height of the GWM against all kinds of observations measured by buoys, ships and satellites from 2012 to 2020. The remarkable improvement of T+0 RMSE in late 2012 corresponds to the implementation of data assimilation. The gradual decrease in RMSEs for the all lead times suggests the improvement of the performance of the JMA's weather and wave prediction systems.
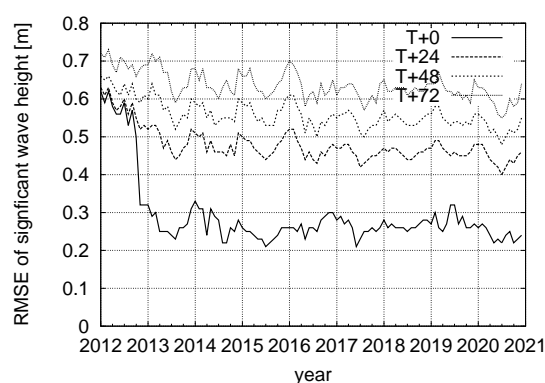
Figure 5.4.8: Time-series representation of analysis and forecast scores for the GWM.

Wave forecast errors are occasionally observed in relation to typhoons. For example:

1. Wave distribution resembling ball pairs sometimes appears due to the bogus wind embedding method.

2. As the model cannot predict asymmetric patterns for typhoons during extratropical transition and similar, initial winds with "bogus wind" need to be improved.

In order to further improve the accuracy of its wave prediction, JMA plans the following developments for the wave models. The grid resolution of the GWM will be enhanced. In future work, a multi-grid model incorporating the GWM, the CWM and a higher resolution wave model for coastal regions of Japan will be operated.

5.5 Storm Surge Model

5.5.1 Japan Area Storm Surge Model

5.5.1.1 Introduction

The Japanese Archipelago is vulnerable to storm surges because of its topography characterized by gulfs open to the south and shallow coasts, making accurate and timely forecasts/warnings crucial in mitigating related threats to life and property.

The Japan Meteorological Agency (JMA), which is responsible for issuing storm surge warnings, has operated a numerical storm surge model since July 1998 to provide basic related information. At first, the model was run four times a day when a typhoon was present in the vicinity of Japan. It is continuously improved, such as enlarging the model domain, predicting extratropical cyclone conditions, extending forecast times, adding advection terms. Since May 2010, a new storm surge model with higher resolution (approx. 1-km mesh near coastal areas) and a gridded astronomical tide analysis method have been operated in storm tide calculation for more practical information and warnings.

5.5.1.2 Dynamics

Storm surges are mainly caused by the effects of wind setup due to strong onshore sea surface winds and inverse barometer effects associated with pressure drops in low-pressure systems. The effects of wind setup are proportional to the square of wind speed and inversely proportional to water depth, and are related to coastal topography, meaning that they are amplified in open bays against the wind.

The JMA storm surge model is similar to the one described in Higaki *et al.* (2009), and is based on two-dimensional shallow water equations driven by meteorological fields. These equations are composed of vertically integrated momentum equations in two horizontal directions:

$$\frac{\partial U}{\partial t} + u\frac{\partial U}{\partial x} + v\frac{\partial U}{\partial y} - fV = -g(D+\eta)\frac{\partial(\eta-\eta_0)}{\partial x} + \frac{\tau_{sx}}{\rho_w} - \frac{\tau_{bx}}{\rho_w} \tag{5.5.1a}$$

$$\frac{\partial V}{\partial t} + u\frac{\partial V}{\partial x} + v\frac{\partial V}{\partial y} + fU = -g(D+\eta)\frac{\partial(\eta-\eta_0)}{\partial y} + \frac{\tau_{sy}}{\rho_w} - \frac{\tau_{by}}{\rho_w} \tag{5.5.1b}$$

and the continuity equation:

$$\frac{\partial \eta}{\partial t} + \frac{\partial U}{\partial x} + \frac{\partial V}{\partial y} = 0 \tag{5.5.2}$$

where U and V are volume fluxes in the x- and y-directions, defined as:

$$U \equiv \int_{-D}^{\eta} u\,dz \tag{5.5.3a}$$

$$V \equiv \int_{-D}^{\eta} v\,dz \tag{5.5.3b}$$

Other notations are as follows. f is the Coriolis parameter; g is gravity acceleration; D is the water depth below mean sea level; η is surface elevation; η_0 is the inverse barometer effect converted into the equivalent water column height; ρ_w is the density of water; τ_{sx} and τ_{sy} are the x- and y-components of wind stress on the sea surface, respectively; and τ_{bx} and τ_{by} are the x- and y-components of the stress of bottom friction, respectively. As for the drag coefficient, adjusted parameterization is adopted in reference to the results of Smith and Banke (1975) and Frank (1984):

$$c_d = \begin{cases} (0.63 + 0.1185W) \times 10^{-3} & (W < 20 \text{ m/s}) \\ \{3.00 + 0.0120(W - 25)\} \times 10^{-3} & (W \geq 20 \text{ m/s}) \end{cases} \tag{5.5.4}$$

where W is wind speed.

The equations are solved via numerical integration using the explicit finite difference method. A staggered (or Arakawa-C) grid (Arakawa and Lamb 1977) is adopted for the grid system.

5.5.1.3 Meteorological Forcing

Dynamically predicted meteorological fields (surface winds and sea-level pressures) by the Meso-Scale Model (MSM) are used as external forcing to drive the storm surge model. Furthermore, when a tropical cyclone (TC) is present around Japan, a simple parametric TC model (hereinafter referred to as the typhoon bogus) is also used as forcing.

The main purpose of introducing the typhoon bogus is to predict storm surges based on JMA's typhoon official forecast which is the most reliable one at the time. However, a single result is still insufficient for risk analysis because storm surges drastically change if TC track changes. Thus, in order to take into account the influence of TC track uncertainty on the occurrence of storm surge, five runs of the storm surge model are conducted with possible TC tracks prescribed at the center of and at four points on the forecast circle within which the TC is forecast to be with a probability of 70% (Figure 5.5.1): Center track (1), Fastest track (2), Rightward-biased track (3), Slowest track (4) and Leftward-biased track (5). These five tracks are used to create meteorological fields with the parametric TC model.
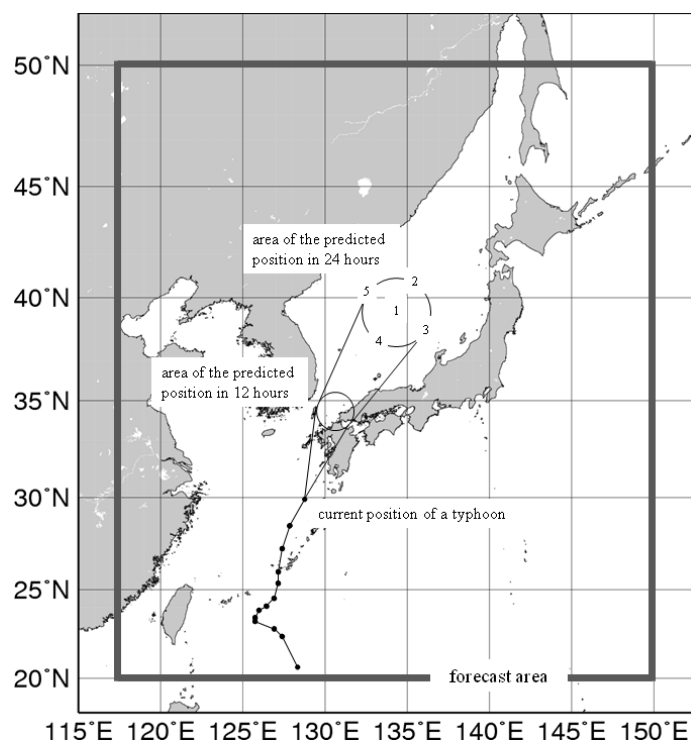

Figure 5.5.1: Bogus TC tracks and the domain of the Japan area storm surge model

The typhoon bogus utilizes Fujita's formula (Fujita 1952), which represents radial pressure distribution in a TC:

$$P = P_\infty - \frac{P_\infty - P_c}{\sqrt{1 + (r/r_0)^2}} \tag{5.5.5}$$

and the gradient wind relation:

$$-\frac{v_g^2}{r} - f v_g = -\frac{1}{\rho_a}\frac{\partial P}{\partial r} \tag{5.5.6}$$

201

In Eq. (5.5.5), P is atmospheric pressure at distance r from the center of the TC, P_∞ is environmental pressure, P_c is the central pressure of the TC and r_0 is a scaling factor for radial distribution of pressure. In Eq. (5.5.6), ρ_a is the density of air and v_g is the gradient wind speed.

To represent the asymmetry of the wind field $\boldsymbol{w}$ in a TC, the moving velocity vector of the TC multiplied by a weight that decays exponentially with distance from the TC center is added to the gradient wind:

$$\boldsymbol{w} = C_1 \left\{ \boldsymbol{v_g} + \boldsymbol{C} \cdot \exp\left(-\pi \frac{r}{r_e} \right) \right\} \tag{5.5.7}$$

$\boldsymbol{C}$ is the TC velocity vector, and r_e is the decay coefficient.

Moreover, an upwind directional land roughness parameterization of Westerink *et al.* (2008) is adopted to represent the wind speed reduction in coastal areas.

TC analysis and forecast information, such as the center position, central pressure and maximum wind, is applied to these formulas to synthesize the wind and pressure fields (Konishi 1995).

5.5.1.4 Model Specifications

Table 5.5.1 gives the specifications of the storm surge model, whose domain covers the whole of Japan (Figure 5.5.1).

<div align="center">Table 5.5.1: Japan area storm surge model specification</div>

Model	two-dimensional model
Grid	Lat-Lon Arakawa-C grid
Region	20°N - 50°N, 117.5°E - 150°E
Resolution	approximately 1, 2, 4, 8, 16 km (Adaptive mesh)
Time step	4 seconds
Initial time	00, 03, 06, 09, 12, 15, 18, 21 (UTC)
Forecast time	51 hours (00, 12 UTC) and 39 hours (03,06,09,15,18,21 UTC)
Member	TC case: 6 members (MSM+5 typhoon bogus)
	no TC case: 1 member (MSM)

Since storm surge is essentially a long wave, its phase speed is proportional to the square root of water depth. It is thus inefficient to set the same resolution for all grids in consideration of computer resources. Accordingly, the Adaptive Mesh Refinement (Berger and Oliger 1984), in which the mesh is fine over shallow water and coarse over deep water, is adopted. The resolution is varied over five levels (1, 2, 4, 8 and 16 km) with water depth (Figure 5.5.2). This method makes storm surge calculation efficient, compared to the normal lat-lon grid system.

The storm surge model runs eight times a day (every 3 hours) and forecasts storm surge up to 51 or 39 hours ahead. Initial values of surface elevation (η) and volume fluxes (U and V) are generated from previous calculation using the newest MSM prediction for forcing, called as hindcast. Since the initial values are not as important as those in atmospheric models, assimilation of observation data is not conducted.

The model computes only storm surges, i.e. anomalies from the level of astronomical tides. However, storm tides (storm surge plus astronomical tide) are required to issue storm surge warnings. Astronomical tides are predicted using harmonic analysis of sea level observations based on JMA's gridded astronomical tide method, in which astronomical tide calculation is performed even for no-observation grid areas (Subsection 5.5.3). After storm surge model computation, the astronomical tide level for the coastal area is simply added to the predicted storm surge.

5.5.1.5 Verification

The accuracy of storm surge prediction depends on the accuracy of the storm surge model itself and atmospheric model conditions. To help eliminate errors of atmospheric model input, the accuracy of the model was evaluated using storm surge predictions driven by atmospheric analysis data.
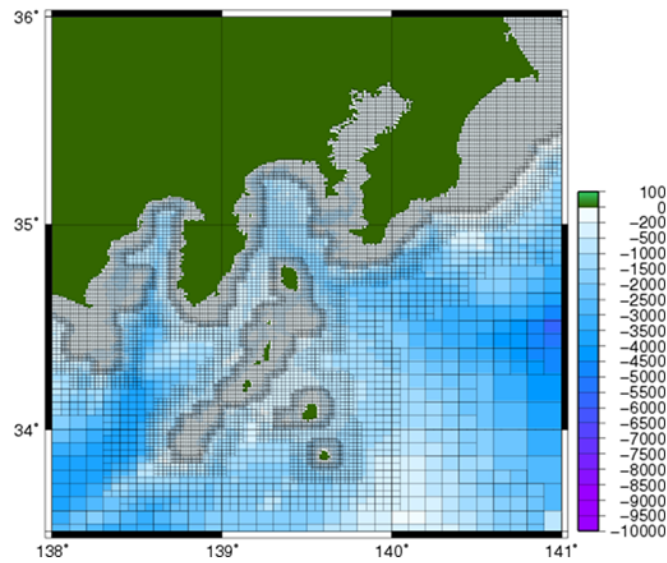
Figure 5.5.2: Storm surge model horizontal grid system and water depth (around the Kanto region)

Figure 5.5.3 shows a scatter diagram of storm surge hindcasts against observation values from 214 tide stations for the statistical period is from June 2015 to December 2020. The stations are managed by organizations including JMA, the Ports and Harbours Bureau, the Japan Coast Guard and the Geospatial Information Authority of Japan. The figure shows that storm surge prediction errors lie in the range of ± 50 cm, although large errors (hindcast values exceeding observation by more than 50 cm) are also observed. It is conceivable that those errors might come from effects which was not included in the storm surge model, such as wave setup, ocean currents and sea water stratification.
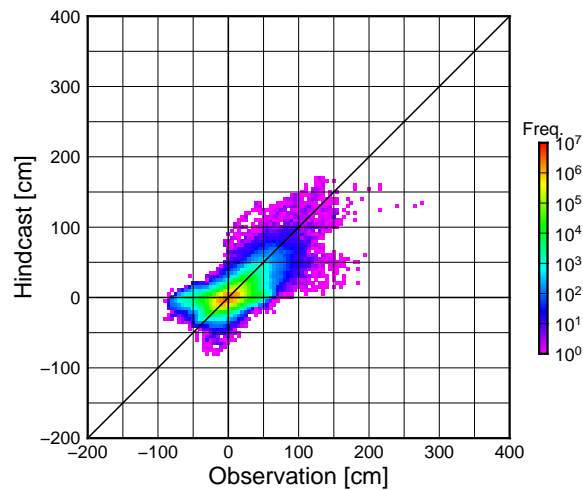

Figure 5.5.3: Scatter diagram of storm surge hindcast values against observed values

Storm surge associated with Typhoon Jebi (T1821) is presented here as an example of related prediction. Figure 5.5.4 shows the track of the typhoon, which passed over central Japan and caused storm surge conditions in Osaka Bay and elsewhere on 4 September 2018. Figure 5.5.5 (a) shows storm surge distribution around the

bay as of 06 UTC on 4 September as predicted by the storm surge model, which reasonably forecasted the large surge behaviors associated with wind setup in the bay's inner part. Figure 5.5.5 (b) shows a time-series chart of storm surge at the port of Osaka. The peak was slightly underestimated and the forecast of its timing was delayed by about an hour, but in general the extreme storm surge conditions were fairly predicted.
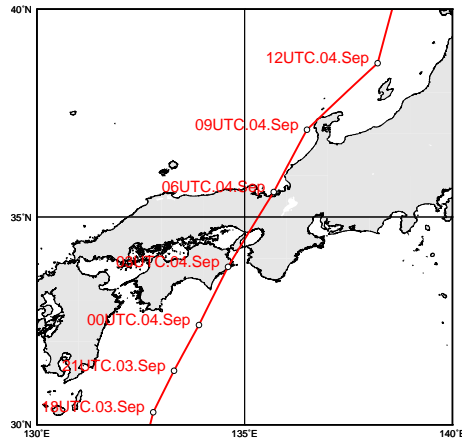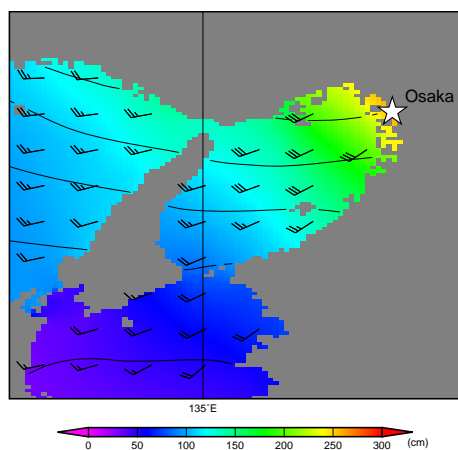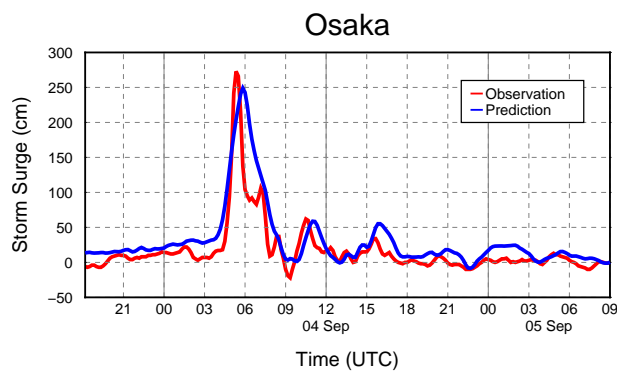

Figure 5.5.4: The track of Typhoon Jebi (T1821)

(a) Distribution of storm surge at 06 UTC on 4 September around Osaka Bay

(b) Time-series chart of storm surge at the port of Osaka

Figure 5.5.5: Storm surge distribution and time-series chart for the port of Osaka as predicted by the storm surge model with an initial time of 18 UTC on 3 September 2018

5.5.2 Asia Area Storm Surge Model

5.5.2.1 Introduction

The late 2000s saw severe storm surge disasters worldwide, including on the coast of the Gulf of Mexico (caused by Hurricane Katrina) in 2005, on the coast of Bangladesh (caused by Cyclone Sidr) in 2007, and on the coast of Myanmar (caused by Cyclone Nargis) in 2008.

In response to a request by the WMO Executive Council (60th session, June 2008), WMO initiated the development of the regional Storm Surge Watch Scheme (SSWS) for areas affected by tropical cyclones. In relation to the western North Pacific and the South China Sea, the ESCAP/WMO Typhoon Committee (41st session, January 2009) endorsed a commitment by the RSMC Tokyo - Typhoon Center to produce storm surge forecasts with the aim of strengthening the storm surge warning capabilities of National Meteorological and Hydrological Services (NMHSs) in the region. JMA began development of a storm surge model for the Asia region in 2010 in collaboration with Typhoon Committee Members providing sea level observation and sea bathymetry data. Horizontal distribution maps of predicted storm surges and time-series charts are published on JMA's Numerical Typhoon Prediction website (Hasegawa *et al.* 2017).

In the last decade, Hurricane Sandy made landfall on the eastern coast of USA in 2012, causing serious damages including the traffic paralysis, massive blackouts and cessation of economic activity in New York. Typhoon Haiyan also caused more than 6,000 fatalities in the Philippines in 2013. Against such a background, storm surge and inundation countermeasures play pivotal roles in efforts to prevent typhoon-related disaster condition.

5.5.2.2 Dynamics

The basic equations of the Asia area storm surge model are similar to those of the Japan area storm surge model (Subsection 5.5.1), but without advection terms. The expressions incorporate vertically integrated momentum fluxes associated with the influence of the earth's rotation with gravity acceleration:

$$\frac{\partial U}{\partial t} - fV = -g(D + \eta)\frac{\partial(\eta - \eta_0)}{\partial x} + \frac{\tau_{sx}}{\rho_w} - \frac{\tau_{bx}}{\rho_w} \tag{5.5.8a}$$

$$\frac{\partial V}{\partial t} + fU = -g(D + \eta)\frac{\partial(\eta - \eta_0)}{\partial y} + \frac{\tau_{sy}}{\rho_w} - \frac{\tau_{by}}{\rho_w} \tag{5.5.8b}$$

and the continuity equation:

$$\frac{\partial \eta}{\partial t} + \frac{\partial U}{\partial x} + \frac{\partial V}{\partial y} = 0 \tag{5.5.9}$$

Definitions of the various variables and constants are as per those of the Japan area storm surge model. Wind stresses are expressed as:

$$\tau_{sx} = c_d \rho_a W u_w \tag{5.5.10a}$$

$$\tau_{sy} = c_d \rho_a W v_w \tag{5.5.10b}$$

where c_d is the drag coefficient, ρ_a is the density of air, $W \equiv \sqrt{u_w^2 + v_w^2}$ is wind speed, and (u_w, v_w) is wind velocity. The drag coefficient is set from the results of Smith and Banke (1975) and Frank (1984):

$$c_d = \begin{cases} (0.63 + 0.066W) \times 10^{-3} & (W < 25 \text{ m/s}) \\ \{2.28 + 0.033(W - 25)\} \times 10^{-3} & (W \geq 25 \text{ m/s}) \end{cases} \tag{5.5.11}$$

5.5.2.3 Data

Bathymetry data for the storm surge model mostly come from 30-second-interval grid datasets of the General Bathymetric Chart of the Oceans (GEBCO 2014) (Figure 5.5.6). These data are partially modified using local bathymetry data provided by Typhoon Committee Members to enable more accurate forecasts.

Astronomical tides are determined via harmonic analysis using past tide observation data provided by Typhoon Committee Members.
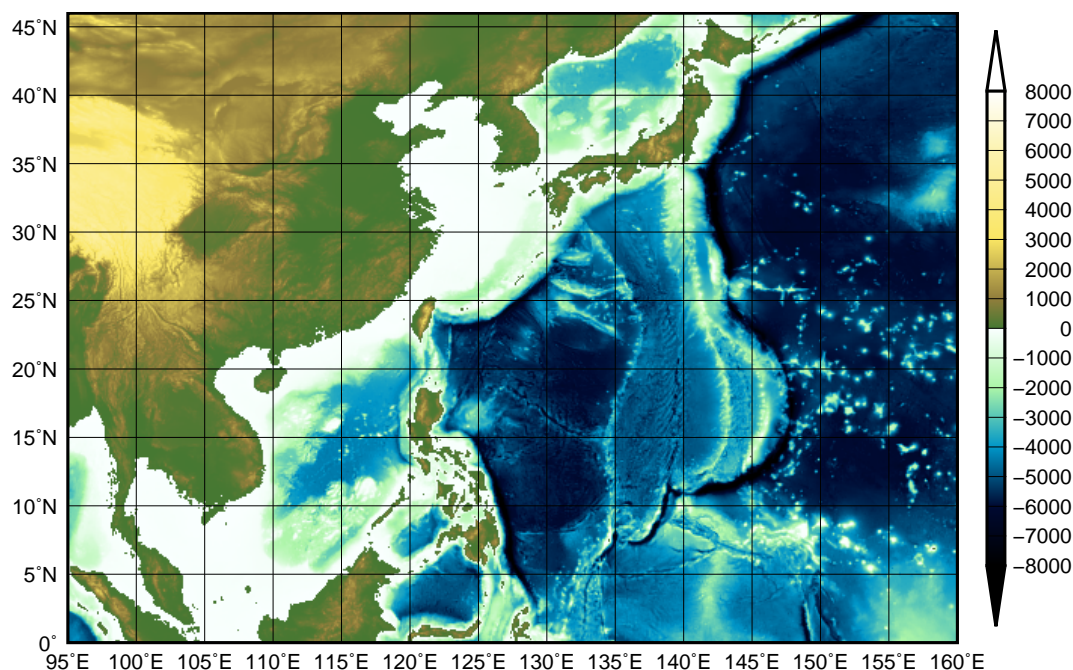

Figure 5.5.6: Model domain and topography of the Asia area storm surge model

5.5.2.4 Meteorological Forcing

Operation of the Asia area storm surge model involves the blending of a simple parametric TC model and output of JMA's operational Global Spectral Model (GSM) as meteorological forcing fields. The simple parametric TC model in this resource is as per that of the Japan area storm surge model (typhoon bogus in Subsection 5.5.1). Related calculation requires an atmospheric model covering the Asian region, but the resolution of the atmospheric model (20 km) is insufficient for adequate expression of TC intensity. Accordingly, meteorological forcing is generated by planting typhoon bogus information into atmospheric model gridded data.

5.5.2.5 Multi-scenario Prediction

Storm surge model calculation was previously based on one scenario involving the GSM and typhoon bogus. However, deterministic forecasting is insufficient for risk management because the occurrence and the intensity of storm surge strongly depend on TC tracks. Against this background, JMA introduced multi-scenario predictions (Hasegawa *et al.* (2017)) determined from the Global Ensemble Prediction System (GEPS) (Kyouda and Higaki (2015)), which has 51 members. To cover the most representative storm surge conditions with minimal calculation, five typical scenarios are selected from all members with cluster analysis (the K-means method):

$$C_k = \frac{1}{N_k} \sum x_i, (k = 1, ..., K) \tag{5.5.12a}$$

$$x_i = (lat_i, lon_i), (i = 1, ..., N) \tag{5.5.12b}$$

where C_k is the cluster center and the TC location, $N = 51$, $K = 5$. Five scenarios are assumed in order to provide appropriate variance for coverage of representative scenarios. As the horizontal resolution of the

GEPS (40 km) is considered too coarse for adequate TC prediction, typhoon bogus is introduced into TC tracks of selected scenarios.

5.5.2.6 Model Specifications

Table 5.5.2 outlines the specifications of the Asia area storm surge model. The horizontal grid resolution is 2 minutes, corresponding to a distance of about 3.7 km. The model covers most of the RSMC Tokyo - Typhoon Center's area of responsibility (Figure 5.5.6), running every six hours and calculating storm surge predictions up to 72 hours ahead. If no TC is present, a single calculation is conducted with GSM prediction. If one or more TCs are present or expected in the model domain, five predictions are carried out based on possible scenarios from the GEPS with wind and pressure fields modified by typhoon bogus.

Three-hourly distribution maps of the whole domain and enlarged versions showing only areas around the TC are available up to 72 hours ahead. The time-series charts provided include data on predicted/astronomical tides, storm surge, sea level pressure and surface wind. Time-series charts for 78 locations are currently provided to Typhoon Committee Members.

Table 5.5.2: Asia area storm surge model specifications

Model	two-dimensional linear model
Grid	Lat-Lon Arakawa-C grid
Region	0° - 46°N, 95°E - 160°E
Resolution	2-minutes mesh (approx. 3.7 km mesh)
Time step	8 seconds
Initial time	00, 06, 12, 18 (UTC)
Forecast time	72 hours
Member	TC case: 6 members (GSM + 5 typhoon bogus)
	no TC case: 1 member (GSM)

5.5.2.7 Verification

To evaluate the performance of the Asia area storm surge model, accuracy was verified by comparing predicted and observed values of hourly storm surge for eight tide stations for the statistical period from 2017 to 2020. Figure 5.5.7 shows a scatter diagram of storm surge hindcasts against observation values. Most storm surge prediction errors lie within the range of ± 50 cm, although some underestimations are detected. The underestimations were results at Quarry Bay (Hong Kong) by Typhoon Mangkhut (T1822), which was an intense typhoon and atmospheric model (GSM) could not resolve sufficient sea level pressures and surface winds. Yearly verification details are provided in the Annual Report on the Activities of the RSMC Tokyo - Typhoon Center [10].

---

[10] http://www.jma.go.jp/jma/jma-eng/jma-center/rsmc-hp-pub-eg/annualreport.html
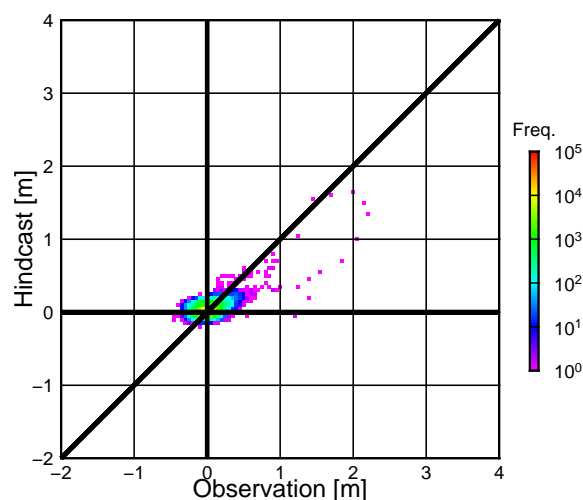
Figure 5.5.7: Scatter diagram of storm surge hindcast values against observation values

Figure 5.5.8 and Figure 5.5.9 show storm surge distribution mapping for Typhoon Hato (T1713) and time-series charts for Quarry Bay (Hong Kong), respectively. The typhoon made landfall on the coast of southern China and generated extremely high storm surges in Hong Kong. The results for Scenario 1 well predict the observation values.

5.5.3 Astronomical Tide Analysis

5.5.3.1 Introduction

The model described in Subsection 5.5.1 calculates only storm surges, defined as anomalies from the astronomical tide level. However, prediction of storm tides (i.e., storm surge plus astronomical tides) is needed for storm surge warning issuance. In 2010, JMA changed its storm surge warning criteria to cover issuance for all coastal areas of Japan in consideration of inundation risk at all points. Appropriate issuance of warnings requires calculation to determine astronomical tides in all coastal areas.

5.5.3.2 Analysis Method

Tidal variations are expressed as a composite of periodic oscillations with various frequencies, as observed with semi-diurnal, diurnal and annual tides. Semi-diurnal and diurnal tides are caused by lunar and solar gravitational forces, while annual tides are brought by seasonal variations in seawater temperature and sea surface pressure. Harmonic constants are sets of amplitudes and phases for individual tidal constituents. Harmonic constants at tide station points can be derived by analyzing hourly tidal observation data, but cannot be determined for arbitrary coastal points where such data are unavailable using this method.

To enable analysis of astronomical tides for the whole of Japan's coast, both short-period (semi-diurnal and diurnal) and long-period tides (annual) tides are considered as shown in Figure 5.5.10. The constituents used in this method (Takasa *et al.* (2011)) are shown in Table 5.5.3.

5.5.3.3 Short-period Tides

Eight major constituents with relatively large amplitudes (K1, O1, P1, Q1, K2, M2, N2 and S2; Table 5.5.3) are estimated using the Oregon State University Tidal Inversion Software (OTIS) tidal model package (Egbert and Erofeeva 2002), which involves data preparation, ocean dynamics and data assimilation. Only the linearized version of ocean dynamics (a tidal model), in which Fourier transform is applied to eliminate time variation, is used:
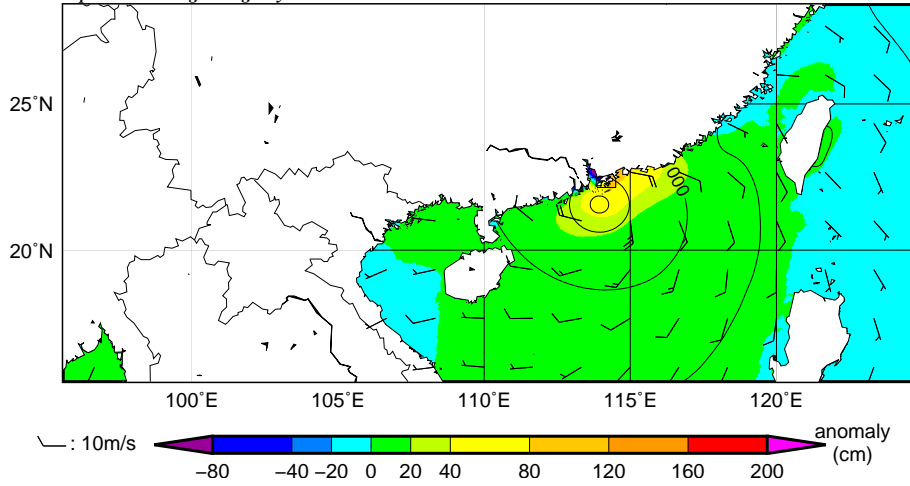
Figure 5.5.8: Distribution of storm surge at 03 UTC on 23 August as predicted by the Asia area storm surge model with an initial time of 00 UTC on 22 August
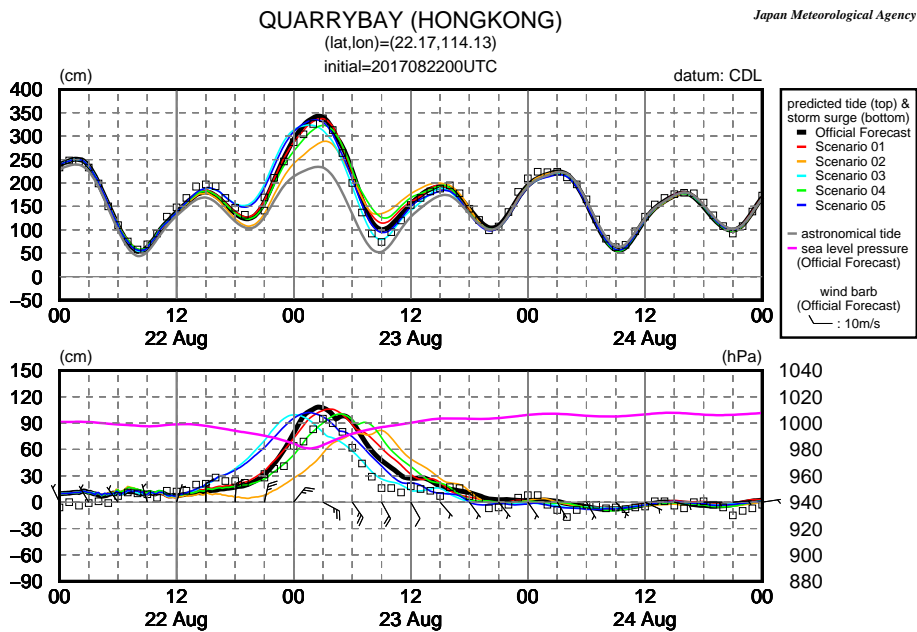

Figure 5.5.9: Time-series charts of storm tide and astronomical tide (top), storm surge, sea level pressure and surface wind (bottom) for Quarry Bay (Hong Kong) as predicted by the Asia area storm surge model with an initial time of 00 UTC on 22 August. Squares show hourly observations.
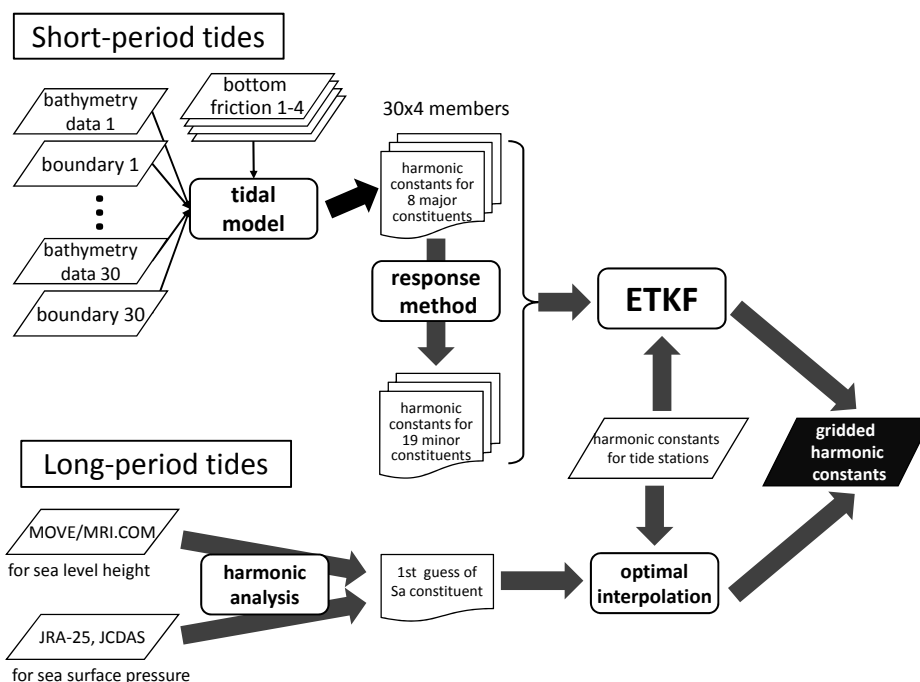
Figure 5.5.10: Flow of astronomical tide analysis

Table 5.5.3: Constituents used in astronomical tide analysis.

Name	Type	Major/Minor	Name	Type	Major/Minor
S_a	annual	-	θ_1	diurnal	minor
$2Q_1$	diurnal	minor	J_1	diurnal	minor
σ_1	diurnal	minor	OO_1	diurnal	minor
Q_1	diurnal	major	$2N_2$	semi-diurnal	minor
ρ_1	diurnal	minor	μ_2	semi-diurnal	minor
O_1	diurnal	major	N_2	semi-diurnal	major
MP_1	diurnal	minor	ν_2	semi-diurnal	minor
M_1	diurnal	minor	M_2	semi-diurnal	major
χ_1	diurnal	minor	λ_2	semi-diurnal	minor
π_1	diurnal	minor	L_2	semi-diurnal	minor
P_1	diurnal	major	T_2	semi-diurnal	minor
K_1	diurnal	major	S_2	semi-diurnal	major
ψ_1	diurnal	minor	R_2	semi-diurnal	minor
ϕ_1	diurnal	minor	K_2	semi-diurnal	major

$$iωU − fV + gH\frac{∂ζ}{∂x} + κU = F_U \tag{5.5.13}$$

$$iωV + fU + gH\frac{∂ζ}{∂y} + κV = F_V \tag{5.5.14}$$

$$\left(\frac{∂U}{∂x} + \frac{∂V}{∂y}\right) + iωζ = 0 \tag{5.5.15}$$

where $ω$ is the tidal constituent frequency, U and V are the x and y components of current integrated from the sea surface to the bottom, respectively, f is the Coriolis parameter, g is gravity acceleration, H is depth, $ζ$ is the anomaly from mean sea level, $κ$ is the dissipation coefficient of bottom friction, and F is the tide-generating force.

The Ensemble Transform Kalman Filter (ETKF) (Bishop *et al.* 2001) is used to assimilate harmonic constants at tide stations. As the model results contain uncertainty due to a lack of resolution and accuracy in bathymetry data and lateral boundary conditions, perturbations are added to these conditions to create an ensemble. There are 30 sets of bathymetry data (incorporating random errors) and boundary condition data generated by blending results from four tidal models (NAO.99Jb (Matsumoto *et al.* 2000), FES2004 (Lyard *et al.* 2006), GOT00.2 (an update to Ray (1999)) and TPXO (Egbert and Erofeeva 2002)). Four sets of bottom friction data are also used in consideration of the influence of such friction on tidal amplitude (Yano *et al.* (2010) and An (1977)). The 120 ensemble members are associated with a combination of the 30 sets of bathymetry and boundary condition data and 4 sets of bottom friction data.

A total of 19 minor constituents (see Table 5.5.3) are estimated from major constituents of similar frequency using the response method (Munk and Cartwright 1966).

5.5.3.4 Long-period Tides

The first guess of annual constituents (S_a) is derived from the results of harmonic analysis of reanalyzed sea level height from MOVE-WNP (see Section 5.3 and Usui *et al.* (2006)) corrected with sea surface pressure from the Japanese 25-year Reanalysis (JRA-25) and the JMA Climate Data Assimilation System (JCDAS) (see Section 2.10 and Onogi *et al.* (2007)) assuming hydrostatic balance. This is modified using harmonic constants for tide stations with the optimal interpolation (OI) method.

5.5.3.5 Verification

To verify astronomical tide analysis based on the method described, the outcomes are compared with those from harmonic constants at tide stations. Figure 5.5.11 shows a comparison of root mean square errors (RMSEs) for the respective distributions. For most stations, the error is less than 3 cm, although larger values are observed for some stations, especially in bays and inland sea areas.
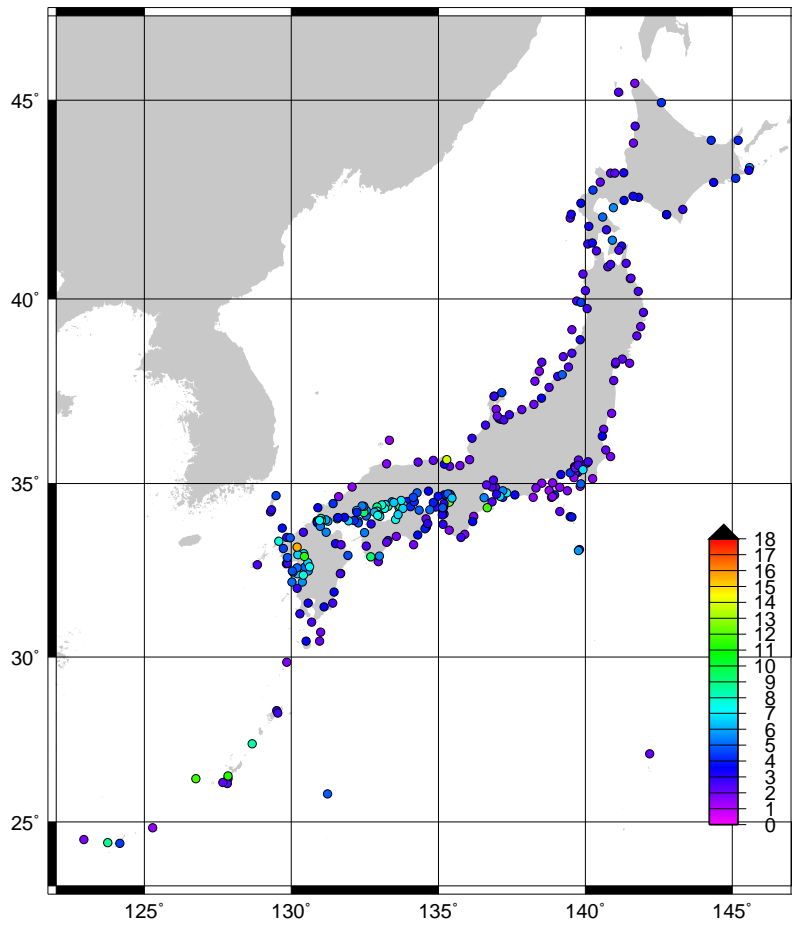
Figure 5.5.11: Distribution of RMSEs from astronomical tide analysis. The unit is cm.

5.6 Sea Ice Model

5.6.1 Introduction

The Japan Meteorological Agency (JMA) has operated a numerical sea ice model since December 1990 to support sea ice forecasting for the southern part of the Sea of Okhotsk in the winter season. Based on dynamics and thermodynamics, the model forecasts distribution and concentration of sea ice for the coming seven-day period. Its output is operationally disseminated twice a week online[11] and via the JMH broadcast system while sea ice is present around Japan's northern island of Hokkaido.

5.6.2 Model Structure

5.6.2.1 Forecast Area

Figure 5.6.1 shows the forecast area, which is a grid of 71×71 squares each with side dimensions representing 12.5km. The model calculates the volume, concentration, velocity and thickness (=volume/concentration) of sea ice for each square based on initial data on sea ice concentration and sea surface temperature (SST), meteorological forecast data and ocean current statistics.
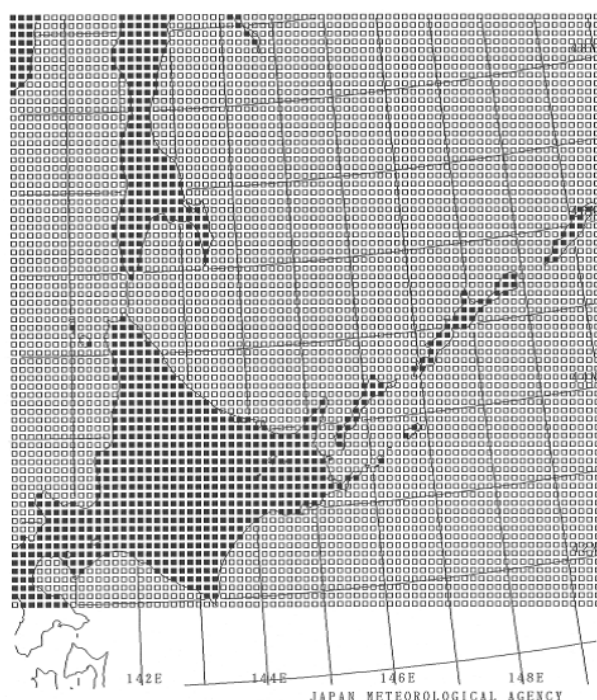

Figure 5.6.1: Forecast area of the sea ice model. ■: land grid square □: sea grid square

5.6.2.2 Calculation of Sea Ice Conditions

The volume (M_i) and concentration (A_i) of sea ice for each grid square are governed by the following equations:

$$\frac{\partial M_i}{\partial t} = -\mathrm{div}(M_i V_i) + P_M$$

$$\frac{\partial A_i}{\partial t} = -\text{div}(A_i V_i) + P_A + D_A \tag{5.6.1}$$

where V_i is sea ice velocity, as determined in the dynamical process described in Subsection 5.6.2.3. P_M and P_A denote changes in volume and concentration, respectively, caused by formation or melting of sea ice and snowfall. These values are determined in the thermodynamic process described in Subsection 5.6.2.4. D_A is a term related to the development of hummocks caused by sea-ice convergence. D_A is given by calculating the convergence of V_i : (Udin and Ullerstig 1976)

$$D_A = \begin{cases} \text{div}(A_i V_i) & A_i = 1 \quad \text{and} \quad \text{div}(V_i) < 0 \\ 0 & 0 < A_i < 1 \quad \text{or} \quad \text{div}(V_i) \geq 0. \end{cases} \tag{5.6.2}$$

5.6.2.3 Dynamical Processes

The momentum equation for sea ice is as follows: (Hibler 1979)

$$\rho_i H_i \frac{\partial V_i}{\partial t} = \tau_a(V_a) + \tau_w(V_w, V_i) + C(V_i) + G(V_w) + F_i \tag{5.6.3}$$

τ_a : wind stress,

τ_w : water stress,

C : Coriolis force,

G : pressure gradient force caused by sea surface tilt,

F_i : internal ice stress.

Here, ρ_i and H_i ($=M_i / A_i$) are sea ice density and thickness, respectively. V_a, V_w, and V_i denote the velocity of wind, ocean currents and sea ice, respectively. As the left-side term of Eq. (5.6.3) is smaller than the other terms by more than one order of magnitude, V_i can be approximated on the assumption that the terms on the right of the equation are in balance. V_a is given by the Global Spectral Model (GSM, see Section 3.2) and V_w is given by the climatology described in Subsection 5.6.3.3. We simplified Hibler's viscous-plastic method to calculate F_i because F_i is such a quite complex term that we used a lot of computational resources. The alternate method is that a provisional sea ice velocity calculated by the assumption that the first four terms of Eq. (5.6.3) are balanced is modified with the non-slip condition for coastal grid squares.

5.6.2.4 Thermodynamic Processes

The thermodynamic processes in the model affect the formation or melting of sea ice caused by heat exchange among the atmosphere, the ocean and sea ice. In the sea ice area, heat exchange between the atmosphere and sea ice causes changes in sea ice thickness. The heat balance equation for the sea ice surface is as follows (Semtner 1976):

$$(1 - Al)R_s \downarrow + R_a \downarrow + SH(T_i) \downarrow + LH(T_i) \downarrow - FL(T_i, H_i) \downarrow - R_i(T_i) \uparrow = 0 \tag{5.6.4}$$

R_s : solar radiation,

Al : albedo of sea ice or snowfall,

R_a : atmospheric radiation,

SH : sensitive heat flux,

LH : latent heat flux,

FL : vertical heat flux in sea ice,

R_i : radiation emitted from sea ice,

T_i : surface temperature of sea ice.

R_s and R_a are given by the GSM, and T_i can be calculated from Eq. (5.6.4). If $T_i < -1.8°C$, sea ice gains thickness in an amount estimated from FL. If $T_i > 0°C$, sea ice loses thickness in an amount estimated from the sum of all terms on the left of Eq. (5.6.4) after T_i is set to 0°C. If $-1.8°C \leq T_i \leq 0°C$, sea ice remains unchanged.

In open water areas, heat exchange between the atmosphere and the ocean causes changes in sea water temperature that affect sea ice melting conditions. The ocean in the model consists of a thin surface layer and a mixed layer. The amount of heat exchange between the ocean and the atmosphere for each grid square is described as follows:

$$Q_w \downarrow = (1 - Al_w)R_s \downarrow + R_a \downarrow + SH(T_s) \downarrow + LH(T_s) \downarrow - R_w(T_s) \uparrow \qquad (5.6.5)$$

Here R_w denotes radiation emitted from the sea surface, and Al_w is the albedo of sea water. T_s is the temperature of the surface layer. Heat exchange between the sea surface layer and the mixed layer is calculated as follows:

$$T_s = \frac{(T_s - T_f)D_s + (T_m - T_f)D_m}{D_s + D_m} + T_f \qquad (5.6.6)$$

Here D_s and D_m denote the depth of the surface layer and the mixed layer, respectively, and are fixed for each sea grid square. T_m is the temperature of the mixed layer, and T_f is the freezing point $(-1.8°C)$ of sea water. Here, calculation of sea water temperature change is based on the assumptions that direct heat exchange between sea ice and sea water occurs only through the surface layer and that heat exchange between sea ice and the surface layer occurs to drive T_s to the melting point (0°C).

5.6.3 Data Used in the Model

5.6.3.1 Initial Data on Sea Ice and Sea Surface Temperature

Initial fields of sea ice concentration are subjectively estimated on the basis of data from satellites (mainly HIMAWARI and NOAA/Metop), aircraft, ships and coastal observations, while initial fields of sea ice thickness are derived from the previous forecast and daily SST analysis data for the seas around Japan (given by MGDSST; Subsection 5.2.1) are used as initial fields for SST.

5.6.3.2 Meteorological Data

Air pressure, air temperature, wind, dew point, solar radiation, atmospheric radiation and precipitation on the sea surface for each grid square are given from interpolation of predictions made by the atmospheric numerical model (GSM).

5.6.3.3 Ocean Current Data

The distribution of ocean currents used in the model is obtained from the Japan Maritime Safety Agency (1983) as shown in Figure 5.6.2. The value is fixed throughout the winter season.

5.6.4 Numerical Sea Ice Model Results

In the example of seven-day forecast results shown in Figure 5.6.3, the model projects that sea ice will move southward to the Sea of Okhotsk coast of Hokkaido.
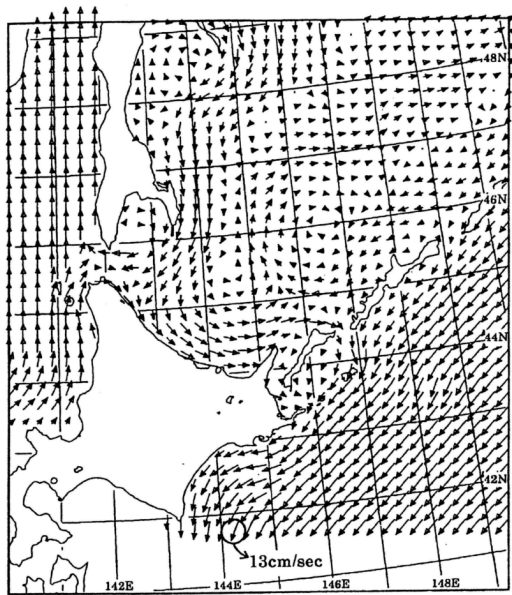
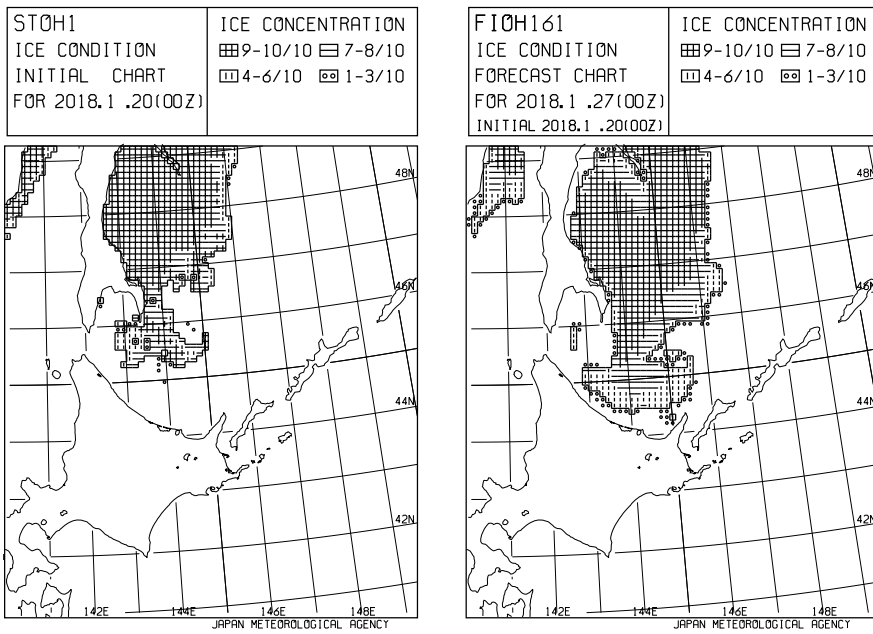Figure 5.6.2: The ocean currents used in the model.

Figure 5.6.3: An example of the results of the model.

5.7 Oil Spill Prediction Model

5.7.1 Introduction

In the 1990s, large-scale oil spills (such as those involving the vessels ABT Summer, MB Braer and Sea Empress) frequently occurred around the world. In Japan, the wrecking of the Russian tanker Nakhodka resulted in a serious oil spill in the Sea of Japan in January 1997, causing major environmental damage along Japan's western coast. Following the Japanese Government's subsequent consideration of countermeasures for large-scale oil spills, JMA has operated its Oil Spill Prediction Model since October 1999.

The model predicts the large-scale behavior of oil spilled in offshore seas. Based on accident information from the Japan Coast Guard, JMA operates the model to produce forecasts with lead time up to 192 hours. The results are provided to personnel responsible for emergency response operations.

The model is applicable to the entire western North Pacific. The domain of calculation is selected from seven settings from $0.8° \times 0.8°$ to $12° \times 12°$ in latitude and longitude based on consideration of incident conditions.

5.7.2 Basic Equation

The oil spill prediction model is generally described by the following equation including terms of advection and diffusion,

$$\frac{dC}{dt} = \frac{\partial C}{\partial t} + \mathbf{V} \cdot \nabla C = \nabla \cdot (K \nabla C) + S \tag{5.7.1}$$

where C is pollutant concentration, t is time, $\mathbf{V}$ is advection velocity, K is the turbulent diffusion coefficient, and S (referred to as the source term) represents the process involved in changing the total amount of oil spilled through changes in oil properties.

Equation (5.7.1) in general can be numerically solved either by calculating C directly using the finite difference method or by simulating the behaviors of a large number of particles representing oil components. The latter approach is used in JMA's Oil Spill Prediction Model. Spilled oil is expressed as numerous particles $C_n (n = 1, 2, \cdots)$ using:

$$C_n \{\mathbf{x}(t + \delta t), s(t + \delta t); t + \delta t\} = \Phi[C_n (\mathbf{x}(t), s(t); t), \delta t] \tag{5.7.2}$$

where $\mathbf{x} = (x, y, z)$ indicates the position of each particle and s is the chemical status of the oil. Φ is a general function describing oil property changes over time.

In the advection term, the effects of surface winds, ocean waves, and ocean currents are taken into account as potentially major factors. Ekman drift current generated by sea surface winds is an example of such as an influence. In the JMA model, surface flows are determined as 2.5% of the wind speed with an angle of $15°$ clockwise with respect to the wind direction. As another example, Stokes drift involves forward movement of particles at the sea surface in the wave direction as a result of wave motion back and forth in each wave cycle. This effect is more significant when high waves are present, and is independent of wind when swell is predominant. Accordingly, Stokes drift is included explicitly and calculated from predictions by JMA ocean wave models. Ocean currents are provided by the JMA Ocean Data Assimilation and Prediction System for the seas around Japan (MOVE-JPN; Subsection 5.3.4).

The three-dimensional diffusion of oil is basically calculated via the shear diffusion treatment proposed by Elliott (1986). Surface flow is assumed to have a logarithmic profile in the vertical direction, and spilled oil is assumed to be carried at a particular horizontal speed in each water level. The shear mechanism is also associated with vertical diffusion. Spilled oil is divided into a large number of droplets with varying levels of buoyancy in line with their size. Consideration of this buoyancy and the present depth of oil drops allows determination of oil motion in the vertical direction and clarification of whether the oil floats on the surface.

In addition to the above shear diffusion process, isotropic diffusion may also be generated by small scale eddies and similar influences as estimated using the constant diffusion coefficient $K_h = 95.0$ m^2/s. As such diffusion may be greater in conditions of strong wind or high waves, the influence is parameterized with additional diffusion coefficients:

Table 5.7.1: Oil Spill Prediction Model specifications

Applicable area		$15°S - 63°N$, $99°E - 80°W$
Domain of calculation		7 options ($0.8° \times 0.8° - 12° \times 12°$)
Grid spacing		7 options (2–30km), according to the domain of calculation
Number of grids		41×41
Prediction period		192 hours
Physical and chemical process	Advection	Ekman drift (estimated from wind field of Global Spectrum Model) Stokes drift (estimated from wave field of Global/Coastal Wave Models) Ocean current (MOVE-JPN)
	Diffusion	Elliott (1986) etc.
	Evaporation	Fingas (2010)
	Emulsification	Reed (1989)

$$
\begin{cases}
\text{waves: } K_{wv} & = 500.0 H_w^2 / T_w \\
\text{winds: } K_{wnd} & = 5.0 W^3 / g
\end{cases}
\tag{5.7.3}
$$

where H_w and T_w are the wave height and period, W is wind speed, and g is gravitational acceleration. The coefficients are empirically determined on the basis of actual cases.

Additional diffusion of oil parcels is estimated from the total value of the diffusion coefficients (K_h, K_{wv}, and K_{wnd}). Specific values are calculated using the random walk method with such diffusion assumed to be horizontal.

Due to the complex behavior of spilled oil, consideration of all related chemical processes is largely impractical. Accordingly, only evaporation and emulsification are considered as major processes. Evaporation is estimated using empirical formulae (Fingas 2010), in which the evaporation rate E_v (%) of most oils can be expressed by the form of either the logarithmic or the root profile over time.

$$
E_v =
\begin{cases}
(a + b \cdot T) \ln t \\
(a + b \cdot T) \sqrt{t}
\end{cases}
\tag{5.7.4}
$$

The constant coefficients a and b are based on experimental results and are listed in the Environment Canada oil data catalogue. T represents oil temperature, and is assumed to be equivalent to sea surface temperature (SST). t is the number of minutes elapsed since the spill.

Emulsification is calculated using the formula of Reed (1989), by which the water content F_{wc} is estimated as:

$$
\frac{dF_{wc}}{dt} = 2.0 \times 10^{-6} (W + 1)^2 \cdot \left(1 - \frac{F_{wc}}{C_3} \right)
\tag{5.7.5}
$$

where W (m/s) is wind speed. C_3 is a constant parameter for the upper limit of water content, and differs among oil types. Oil density is also calculated in consideration of water content, which can change the behavior of oil.

The specifications of the Oil Spill Prediction Model and related processes are summarized in Table 5.7.1.

5.7.3 Products

The model is operated in the event of a large-scale oil spill in offshore deep-water seas, where short-term tidal currents can be negligible. The results of oil spill prediction are provided to the Japanese Government and/or the Japan Coast Guard along with various marine meteorological charts. An example of prediction is shown in Figure 5.7.1.

(a)Forecast period: 24 h

(b)Forecast period: 48 h

(c)Forecast period: 72 h

(d)Forecast period: 96 h

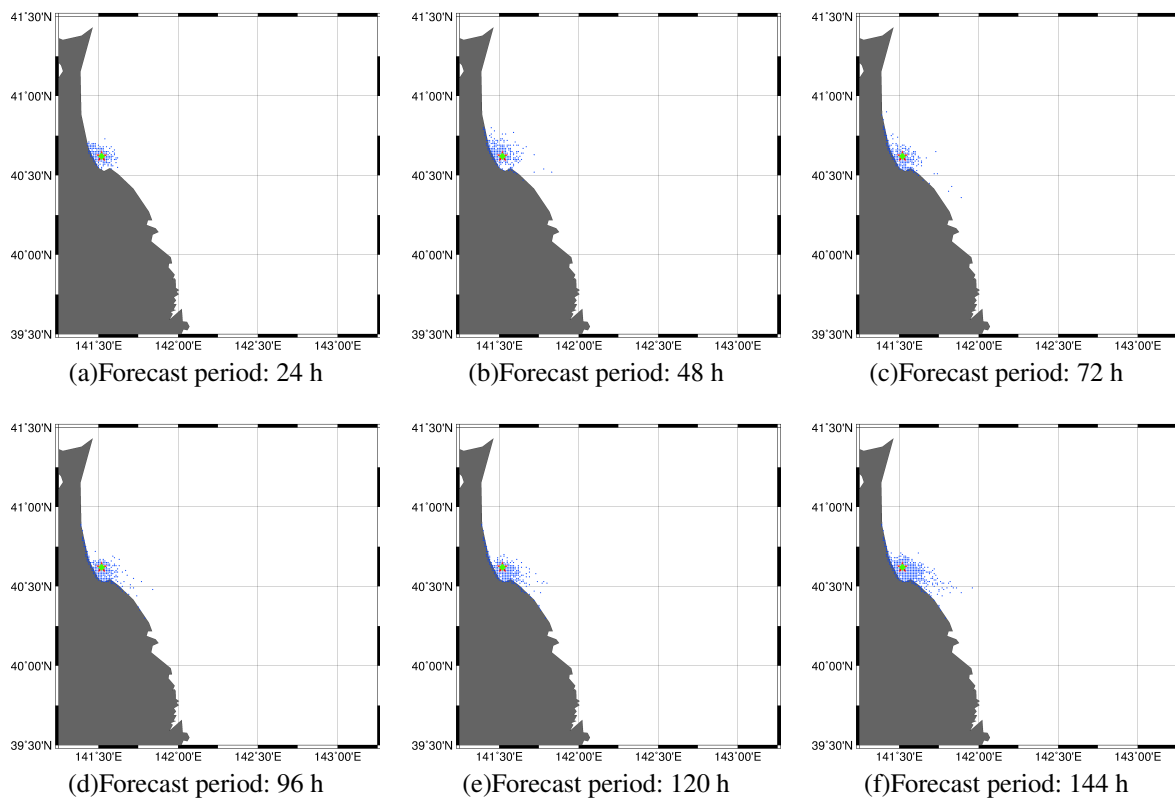(e)Forecast period: 120 h

(f)Forecast period: 144 h

Figure 5.7.1: A simulation for the sea east of Japan supposing an accident at 19UTC on 11 Aug 2021 at 40.37 °N 141.31 °E. The stars show the accident location, and the rhombuses show the source of the spillage (assuming the source is carried by ocean currents). The area and amount of spilled oil are indicated by dot distribution.